# IDŐJÁRÁS

QUARTERLY JOURNAL
OF THE HUNGARIAN METEOROLOGICAL SERVICE

## CONTENTS



*******

http://www.met.hu/Journal-Idojaras.php

VOL. 112 * NO. 1 * JANUARY – MARCH 2008

# IDŐJÁRÁS

*Quarterly Journal of the Hungarian Meteorological Service*



*Editorial Office: Gilice tér 39, H-1182 Budapest, Hungary*
*P.O. Box 39, H-1675 Budapest, Hungary*
*E-mail: bozo.l@met.hu or antal.e@met.hu*
*Fax: (36-1) 346-4809*

**Covered in the abstract and citation database SCOPUS®**

*Subscription by*

*mail: IDŐJÁRÁS, P.O. Box 39, H-1675 Budapest, Hungary;*
*E-mail: kenderesy.k@met.hu or antal.e@met.hu*

# IDŐJÁRÁS

*Quarterly Journal of the Hungarian Meteorological Service*
*Vol. 112, No. 1, January–March 2008, pp. 1–13*


# Thunderstorm climatology analyses in Hungary using radar observations


**Ákos Horváth[1]•, Ferenc Ács[2] and András T. Seres[2]**

[1]*Hungarian Meteorological Service,*
*Vitorlás u. 17, H-8600 Siófok, Hungary; E-mail: horvath.a@met.hu*

[2]*Department of Meteorology, Eötvös Loránd University,*
*P.O. Box 32, H-1518 Budapest, Hungary*



*(Manuscript received in final form November 30, 2007)*



**Abstract—**This paper presents the results of an objective analysis, which deals with thunderstorm-climatology. The aim of this study is twofold: firstly, to describe the space and time distribution of severe thunderstorms in Hungary using radar data in the five-year period of 2003–2007, and secondly, to analyze the relationship between severe thunderstorms and macrosynoptic circulation types. We have applied *Péczely's* (1957) synoptic circulation types. The core of the examination is the modified TITAN (Thunderstorm Identification, Tracking, Analysis, and Nowcasting)-method (*Dixon* and *Wiener*, 1993), where thunderstorms are represented with ellipses (thunderstorm-ellipses). Severe and highly severe thunderstorm-ellipses and stormy days are defined. Most of the severe and highly severe stormy days were associated with typical synoptic situations: prefrontal warm sectors of active cyclones, cold fronts, and anticyclone edges. The detected thunderstorm-ellipses had maxima in the south-west, north, and east parts of Hungary. The results of this examination may be important for forecasting severe thunderstorms, so damage and loss can be reduced.



*Key-words*: thunderstorms, radar, TITAN-method, climatology, Hungary, Péczely-classification


## *1. Introduction*

The information society of today has a growing demand for weather forecasts; interest in the examination of severe thunderstorms has grown rapidly. The climatological aspects of these phenomena have become more common worldwide. In these studies, we have used visual observations and


• Corresponding author

measurements (*Manohar* and *Kesarkar*, 2003), satellite images (*Banta* and *Schaaf*, 1987), lightning tracking systems (*Watson et al*., 1994; *Shwehdi*, 2005), soundings (*Craven* and *Brook*s, 2004), weather and climate models (*Ziegler et al*., 1997; *Schär et al*., 1999), and meteorological radar data. In this study, an approach based on radar data has been presented.

Radar data-based thunderstorm climatology studies appeared for the first time in the USA in the 1950s (*Braham*, 1958). These investigations refer to different regions of the United States (*Myers*, 1964; *Kuo* and *Orville*, 1972; *Henz*, 1974; *Falconer*, 1984; *Croft* and *Shulman*, 1989; *Geerts*, 1997; *MacKeen* and *Zhang*, 1999). Nevertheless, in recent decades there have also been studies referring to South America (*Paiva Pereira* and *Rutledge*, 2003), Canada (*Brimelow et al*., 2004), Australia (*Steiner* and *Houze*, 1996), and Europe (*Jaeneke*, 2001; *Rigo* and *Liasat*, 2002).

The first study in Hungary considering thunderstorms from a climatological point of view was carried out by *Héjas* (1898; 1909) and *Raum* (1910). Héjas examined the relationship between atmospheric pressure systems and the distribution in space of thunderstorms. This investigation is based on visual observations and measurements. Many studies dealing with different aspects of thunderstorm climatology appeared in the 1960s (*Adámy* and *Máhr*, 1963; *Ozorai*, 1965; *Götz* and *Pápainé*, 1966, 1967). Götz and Pápainé examined the distribution of thunderstorms in both the summer and winter seasons using data from a 10-year period. All these studies used data obtained by visual observations. In recent years, there have also been studies (*Horváth* and *Geresdi*, 2000; *Bodolainé* and *Tänczer*, 2005; *Horváth et al*., 2007), which consider thunderstorms from dynamical and synoptical points of view. In these Hungarian studies, there were no radar data-based analyses.

The aim of this study is twofold: firstly, to describe the space/time distribution of severe thunderstorms in Hungary using radar data in the 5-year period of 2003–2007, and secondly, to analyze the relationship between severe thunderstorms and synoptic circulation patterns. *Péczely's* (1957) classification for synoptic patterns has been applied. The analysis reveals which locations are most endangered by thunderstorms and which synoptic patterns are beneficial to severe convective weather. In the first part of the study radar measurements and the localization method (TITAN-method) of thunderstorms are described. The TITAN-method was applied to detect severe and highly severe thunderstorms and their space/time distribution. The relationship was made between Péczely synoptic classes and objectively detected severe thunderstorms.

## *2. Methodology*

### *2.1. Radar measurements*

We used the radar network of the Hungarian Meteorological Service (HMS). Hungary is covered by three radars: the western, the central, and the eastern

radar. In 2003 only two radars provided observations: the western MRL-5 type, in Szentgotthárd-Farkasfa and the central Doppler type in Budapest-Pestszentlőrinc. The eastern, which is located in Nyíregyháza-Napkor, was not in continuous operation because of modernization work being carried out, therefore, there was no reliable information from the north-eastern parts of Hungary in this year. In 2004–2007 Doppler radar measurements covered the whole region (the western radar also changed to Doppler instrumentation and was moved to Pogányvár). All 3 radars operate on the C band (5 cm).

In this study only Doppler radar reflectivity was used. During the measurement procedure the Doppler wind was also applied for noise filtering and quality upgrading, and the composite fields resulted from the upgraded, filtered and smoothed data from the 3 radars. Composite image resolution is $2\,\mathrm{km} \times 2$ km in space and 15 minutes in time. To additionally reduce measurement noise, the median-filter method was also used before beginning the analysis.

### *2.2. The core of the methodology: The modified TITAN-method*

TITAN-method was developed by *Dixon* and *Wiener* (1993). In this study we used the first part of this system: the thunderstorm identification. Using the method, irregular-shaped thunderstorms can be characterized by regular ellipses. The main point of identification is as follows: the parameters of the ellipses are determined by the covariance matrix of the isolated, irregular-shaped cluster on the image using the condition that the area of the cluster has to be equal to the area of the ellipse. The center of a cluster is defined by

$$\overline{x} = \frac{1}{n}\sum_{i=1}^{n} x_i\,, \qquad \overline{y} = \frac{1}{n}\sum_{i=1}^{n} y_i\,, \tag{1}$$

where $x$ and $y$ indicate the longitude and latitude of the relevant pixels (pixels which have reflectivity higher than a threshold value). The covariance of the cluster is

$$A = \mathrm{cov}_{xy} = \begin{bmatrix} d & e \\ e & f \end{bmatrix}, \tag{2}$$

where $d$ is the deviation from the center of the $x$ coordinate

$$d = \frac{1}{n-1}\sum_{i=1}^{n}(x_i - \overline{x})^2. \tag{3}$$

$f$ is the deviation from the center of the $y$ coordinate

$$f = \frac{1}{n-1}\sum_{i=1}^{n}(y_i - \overline{y})^2, \tag{4}$$

while $e$ is

$$e = \frac{1}{n-1}\sum_{i=1}^{n}(x_i - \overline{x})(y_i - \overline{y}). \tag{5}$$

The parameters of the ellipse can be estimated by calculating the eigenvector and eigenvalue of this covariance matrix. These parameters are as follows: the coordinates of the center, the length of the minor and the major axes, and the orientation angle (the angle between the major axis and the $x$ axis). With these parameters, the focus points and the equation of the ellipse can be easily determined, and so the ellipse can be visualized (*Fig. 1*).

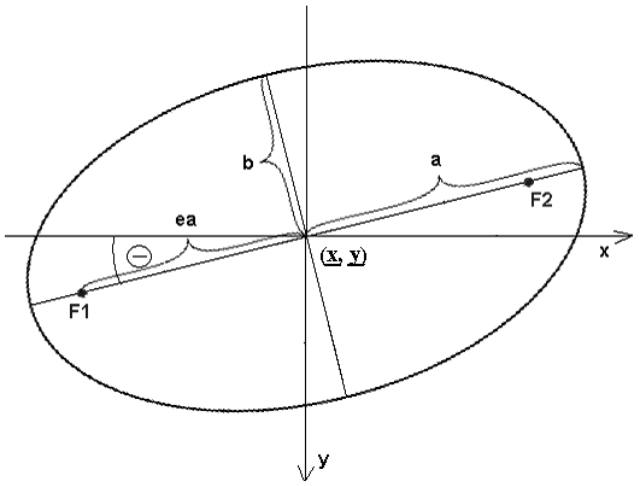


*Fig. 1.* Characteristics of the thunderstorm-ellipse: $\underline{x}$ and $\underline{y}$ are the coordinates of the centre, $a$ is the half of the major axis, $b$ is the half of the minor axis, *F1* and *F2* are the focus points, $\Theta$ is the orientation angle.

These "estimated ellipses" are called *thunderstorm-ellipses*. In carrying out the analysis, the noises were reduced. Two types of thresholds: *the area* ($N_{minlimit}$) and *the value threshold* ($P_{minlimit}$) are defined. The area threshold determines the minimum area of a cluster. In our examination $N_{minlimit}$ is set to be 5 radar pixels (20 km$^2$). The value threshold specifies that the values of all the individual pixels of the cluster (in our case 5 pixels) have to reach this limit. In our examination $P_{minlimit}$ is set to 45 (so-called severe thunderstorm-ellipses) or 50 dBZ (so-called highly severe thunderstorm-ellipses). Using these thresholds, small and weak objects are eliminated. *Fig. 2* shows the ellipses. The original radar image is presented in *Fig. 2a* for May 18, 2005, 14:45 UTC, while the thunderstorm-ellipses are presented in *Fig. 2b*, where $N_{minlimit}$ is 5 radar pixels (20 km$^2$) and $P_{minlimit}$ is 45 dBZ. In this case two isolated convective systems went through Hungary. These systems produced numerous serious convective

phenomena: for example a supercell near Lake Balaton (to the west of the Danube) and near Hortobágy. The latter caused a tornado not far from Hosszúpályi (*Horváth*, 2005).

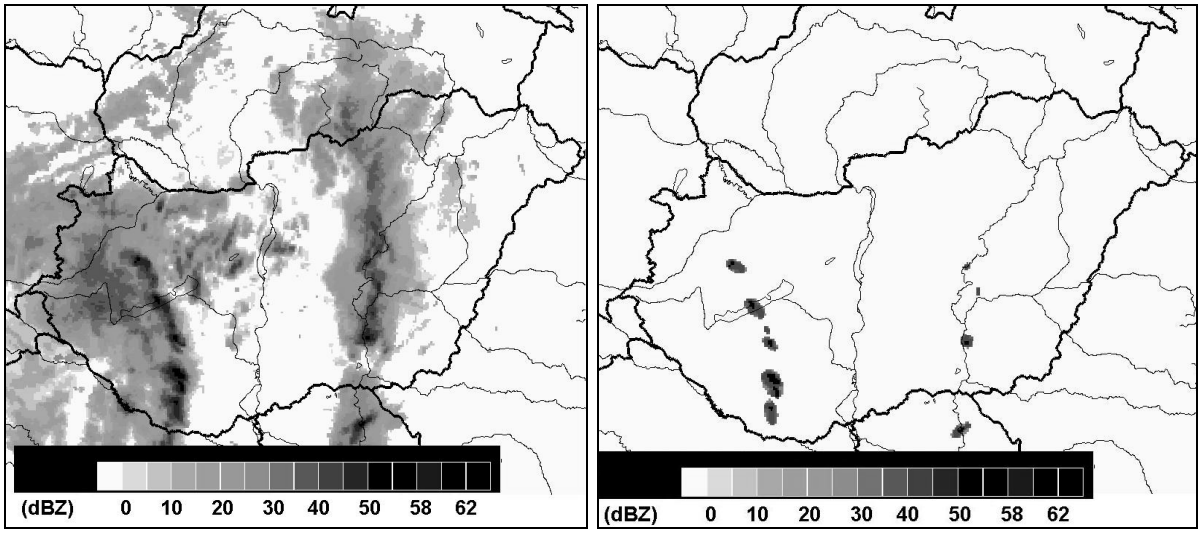


*Fig. 2*. Radar echo pictures of the thunderstorms observed on May 18, 2005, 14:45 UTC. Left: original picture, right: picture where thunderstorms are represented by ellipses.

## *3. Results*

### *3.1. Severe and highly severe stormy days and thunderstorm seasons*

A day is denoted as a *severe or a highly severe stormy day* when at least one detected severe ($P_{minlimit}$ = 45 dBZ) or highly severe ($P_{minlimit}$ = 50 dBZ) thunderstorm ellipse can be found on radar images, and at least one thunderstorm was visually observed by the Hungarian synoptic station network. Visual observations were taken from the *Időjárási Napijelentés* (2003–2007) of the Hungarian Meteorological Service. Using these data the time distribution of stormy days (*Fig. 3*) can be determined, and the number of these days can be counted for each year (*Table 1*).

The most severe stormy days were in 2006, while the most highly severe days occurred in 2007. Note that in 2007, the last three months (October, November, and December) were not processed, therefore, this short period is not presented. 2003 is also shown, but this year is not representative because of the missing reliable radar measurements in the eastern parts of Hungary. From *Fig. 3* it is obvious that in 2003 and 2005 severe and highly severe stormy days appeared mostly in July. In 2004 and 2007, severe and highly severe stormy days appeared mostly in June, while in 2006 these days occurred mostly in August. It is obvious that most severe and highly severe stormy days and thunderstorm-ellipses appeared between April and September, therefore this period is denoted as a *thunderstorm season*.

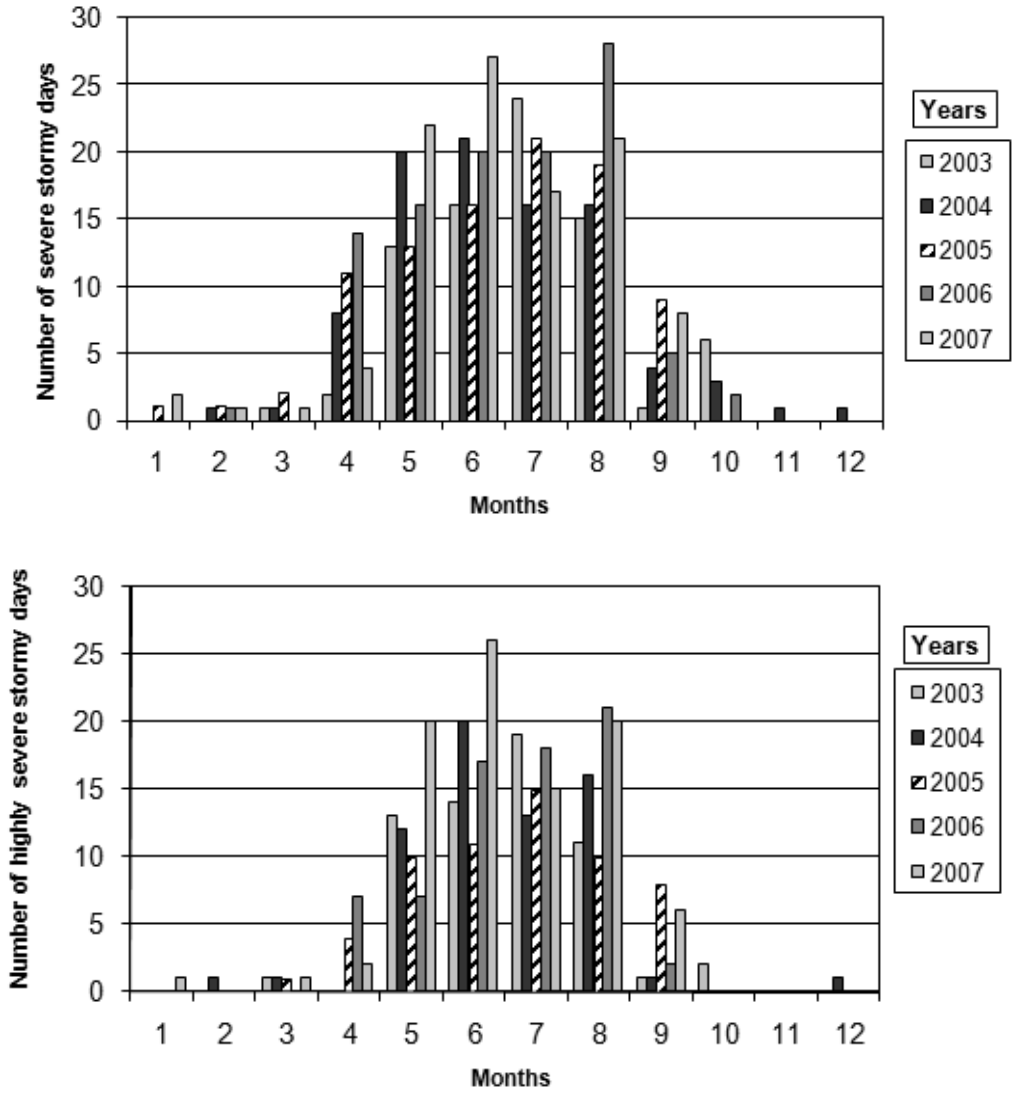


*Fig. 3.* Annual course of (up) severe and (down) highly severe stormy days in the years 2003, 2004 2005, 2006, and 2007. Note that in 2007 only the 9-month period from January to September was processed.

*Table 1.* Number of the severe and highly severe stormy days in the years 2003–2007

| **Years** | **Number of severe stormy days** ($P_{minlimit}$ = 45 dBz) | **Number of highly severe stormy days** ($P_{minlimit}$ = 50 dBz) |
|---|---|---|
| 2003 | 78 | 61 |
| 2004 | 92 | 65 |
| 2005 | 93 | 59 |
| 2006 | 106 | 72 |
| 2007 | 103 | 91 |

*3.2. Spatial distribution of thunderstorm ellipses*

The spatial distribution of thunderstorms is analyzed by constructing *thunderstorm statistic maps*. The maps show the spatial distribution of severe and highly severe thunderstorm ellipses. Note that these calculated values are not equal to the number of the thunderstorms (they are proportional to it, however), because a severe thunderstorm may occur on subsequent radar images. Thunderstorm statistic maps were made for all of the five years from 2003 to 2007 by using the abovementioned different pixel limits ($P_{minlimit} = 45$ or $P_{minlimit} = 50$) for Hungary. The maps were made only for the thunderstorm season period. (In the winter period, there were only a few thunderstorm-ellipses and the measurement noises were high.)

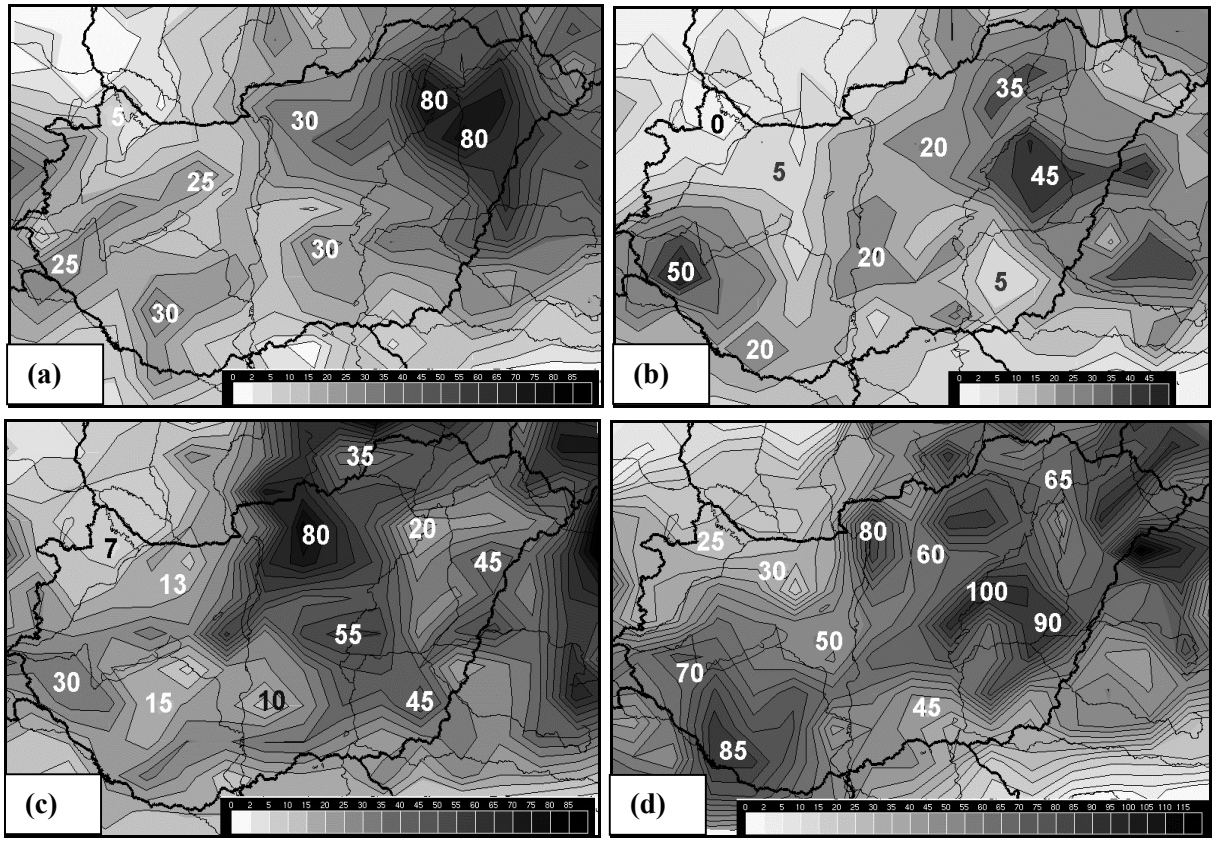


*Fig. 4.* Spatial distribution of severe (at least 45 dBZ) thunderstorm-ellipses in the thunderstorm season of (a) 2004, (b) 2005, (c) 2006, and (d) 2007. The resolution is 30 km × 30 km. These images were visualized by the HAWK system (Hungarian Advanced Workstation).

In 2003, the maxima of severe or highly severe thunderstorms were in the middle parts of Hungary and in the western-central regions to the west of the Danube (not shown). In 2004 the area density maximum is located in the east, north-east part of Hungary. Less severe thunderstorms occurred to the west of the Danube or in the southern regions of the country (*Figs. 4a* and *5a*). In 2005 most of the severe and highly severe thunderstorm-ellipses were located in the

south-west and north-east regions of Hungary, while only a few severe convective objects appeared in the north-west, central, and south-east parts of the country (*Figs. 4b* and *5b*). In 2006 the maxima were in the central-northern parts of Hungary, while less severe and highly severe thunderstorm-ellipses occurred to the west of the Danube (especially in the north-western parts) and in the southern regions (*Figs. 4c* and *5c*). In 2007 most of the severe and highly severe thunderstorm-ellipses were located in the central-eastern and south-western regions of Hungary (*Figs. 4d* and *5d*).

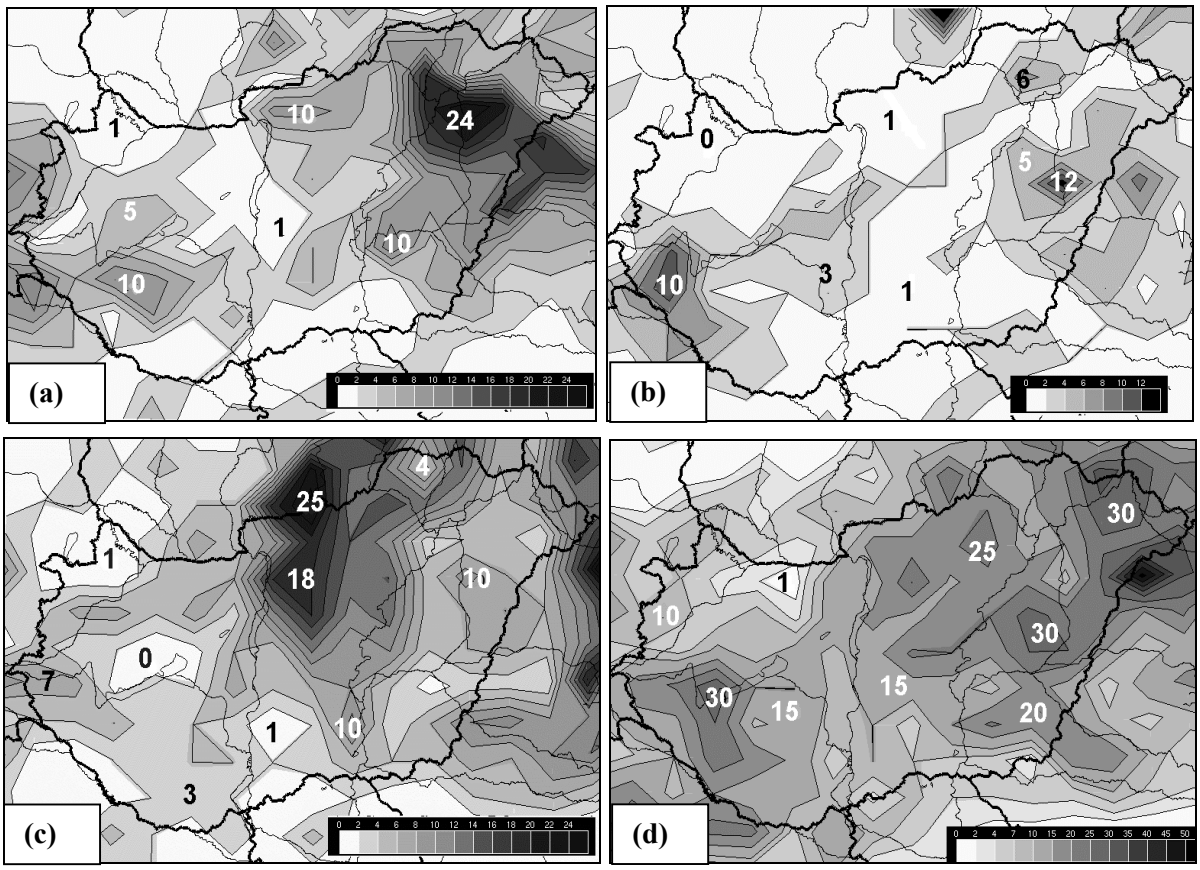


*Fig. 5.* Spatial distribution of severe (at least 50 dBZ) thunderstorm-ellipses in the thunderstorm season of (a) 2004, (b) 2005, (c) 2006, and (d) 2007. The resolution is 30 km × 30 km. These images were visualized by the HAWK system (Hungarian Advanced Workstation).

### *3.3. Frequency distribution of severe and highly severe stormy days according to Péczely's synoptic circulation types*

The relation between stormy days and the synoptic patterns were analyzed by investigating the frequency distribution of severe and highly severe stormy days according to *Péczely's* (1957) synoptic circulation types. The Péczely classification was created to describe the weather patterns especially for Central Europe. Synoptic circulation types were diagnosed from the maps of the published daily weather reports.

Severe and highly severe stormy days in all the years appeared most frequently in the circulation types 4, 1, 6, and 9. Type 11 was quite frequent in 2004 and the type 13 appeared more frequently in 2005. The frequency of appearance of the other types was much smaller (*Fig. 7*). In the circulation type 4, Hungary is in advance of the cold front or in the warm sector (so called pre-frontal situation), which belongs to western/northern cyclones. The type 6 also represents a pre-frontal situation, but in this case the cold front belongs to a Mediterranean cyclone. The type 1 represents situations when the weather of the Carpathian Basin is controlled by a cold front which belongs to a northern cyclone. Type 9 is associated with a western anticyclone, when Hungary is located on the eastern edge of the anticyclone. Type 11 is associated with an anticyclone above Scandinavia, when our region is located on the edge of this anticyclone. On many occasions types 9 and 11 can also be post-frontal, when a western or northern anticyclone develops behind the cold front. The type 13 is associated with cyclones/shallow cyclones above the Carpathian Basin.

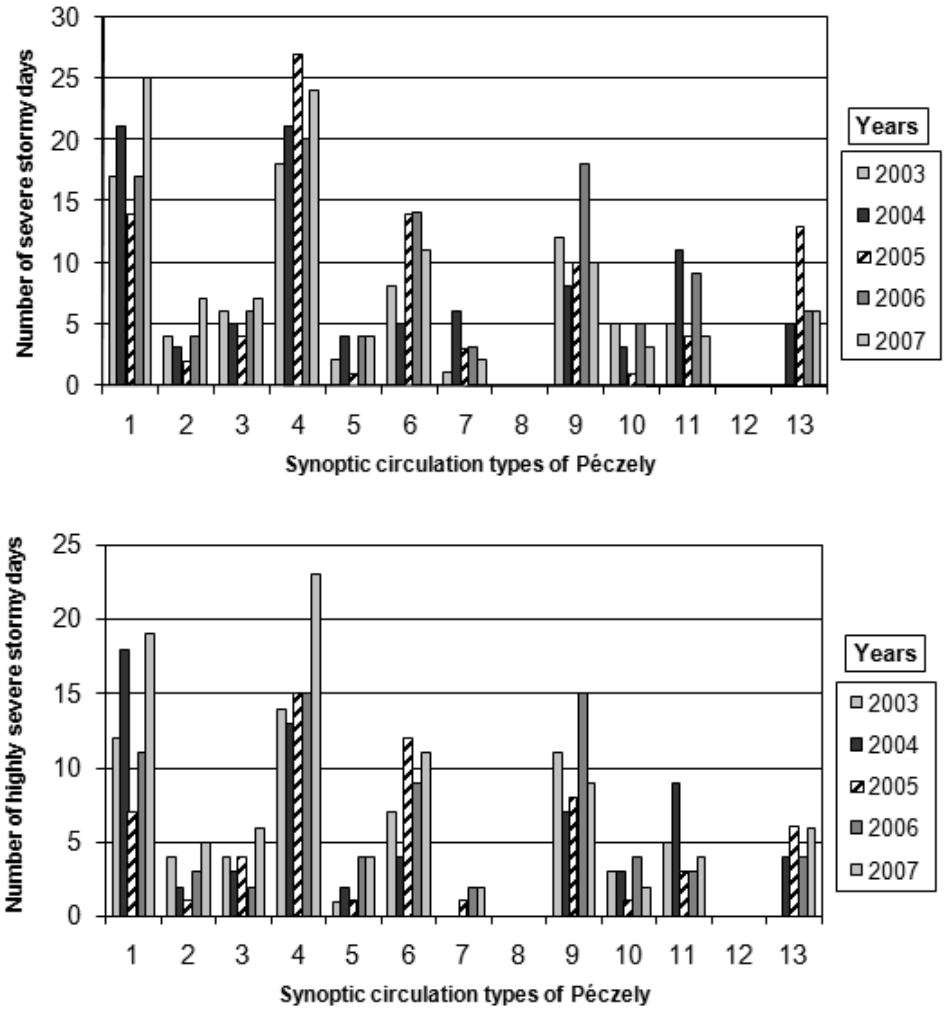


*Fig. 6.* Frequency distribution of (up) severe and (down) highly severe stormy days according to Péczely's synoptic circulation types in the years 2003, 2004, 2005, 2006, and 2007.

### *3.4. Frequency distribution of the detected thunderstorm-ellipses according to Péczely's synoptic circulation types*

To determine the frequency distribution, the number of detected thunderstorm-ellipses of the stormy days has to be counted. Two main groups of *severe stormy days* can be defined: *days with few* and *days with many ellipses* (the number of the detected thunderstorm-ellipses does not exceed or does exceed 50). The frequency distribution of these two different types of severe stormy days is presented in *Fig. 7*. In all examined years, severe stormy days with few thunderstorm-ellipses appeared most frequently in the synoptic circulation types 4, 1, and 9. In one or two years, type 6 (in 2006), type 11 (in 2004 and 2006), and type 13 (in 2005) were frequent (*Fig. 7a*). Considering days with many severe thunderstorms, in 2003 the highest frequency distributions appeared in the circulation types 1 and 4. In 2004 the types 1 and 4, in 2005 the types 4 and 6, in 2006 the types 4 and 9, and in 2007 the types 1, 4, and 6 possessed the highest frequency distributions (*Fig. 7b*).

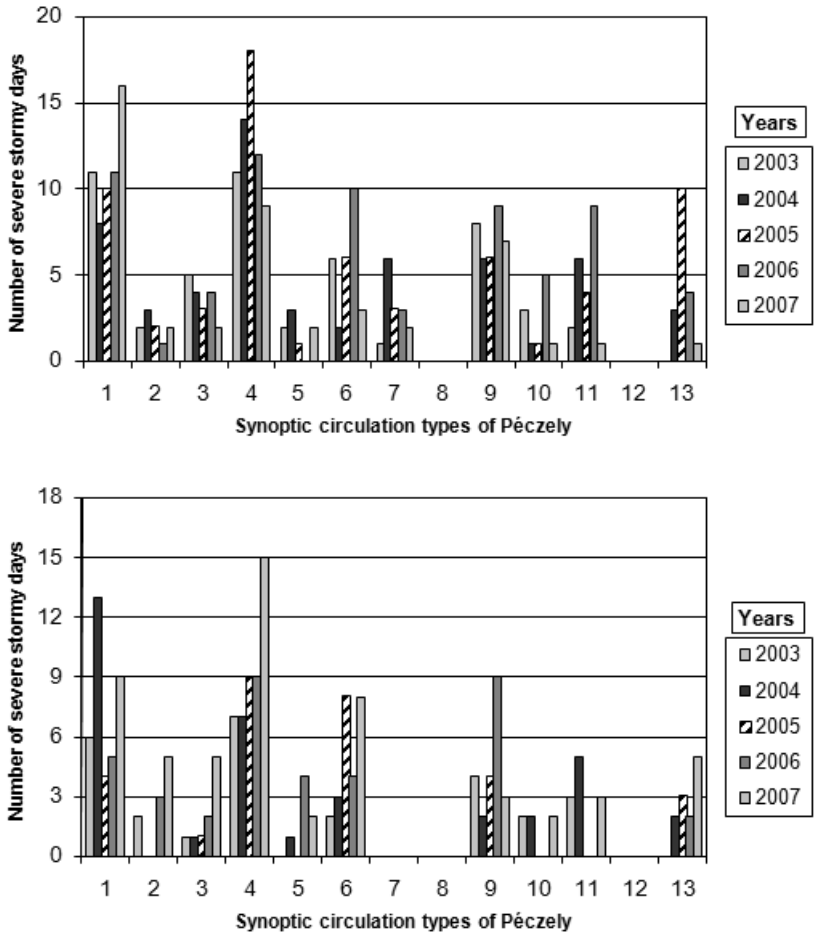


*Fig. 7.* Frequency distribution of severe stormy days with (up) few (the number of thunderstorm-ellipses does not exceed 50) and (down) many (the number of thunderstorm-ellipses exceeds 50) thunderstorm-ellipses according to Péczely's synoptic circulation types in the years 2003, 2004, 2005, 2006, and 2007.

Analogously to severe stormy days, two main groups of *highly severe stormy days* can be defined: *days with few* and *days with many ellipses* (the number of the detected thunderstorm-ellipses does not exceed or does exceed 50) (*Fig. 8*). Highly severe stormy days with few ellipses appeared most frequently in the synoptic circulation types 1, 4, and 9. The appearance was also quite frequent in synoptic circulation types 6 (mainly in 2005), 3 (in 2004 and 2005), and 11 (especially in 2004) (*Fig. 8a*). Except for the years 2004 and 2005, the most highly severe stormy days with many thunderstorm-ellipses were caused by the synoptic circulation type 4. In 2004, the type 1 was the most frequent. In 2005, there were no highly severe stormy days with many ellipses. Highly severe stormy days with many ellipses appeared also, but with lower frequency, in the circulation types 2, 3, 5, 6, 9, and 13 (*Fig. 8b*). Note the high number of highly severe stormy days in 2007! The type 2 is associated with an anticyclone above the British Isles, the 3 with cold fronts of a Mediterranean cyclone, and the 5 with the edge of an eastern anticyclone.

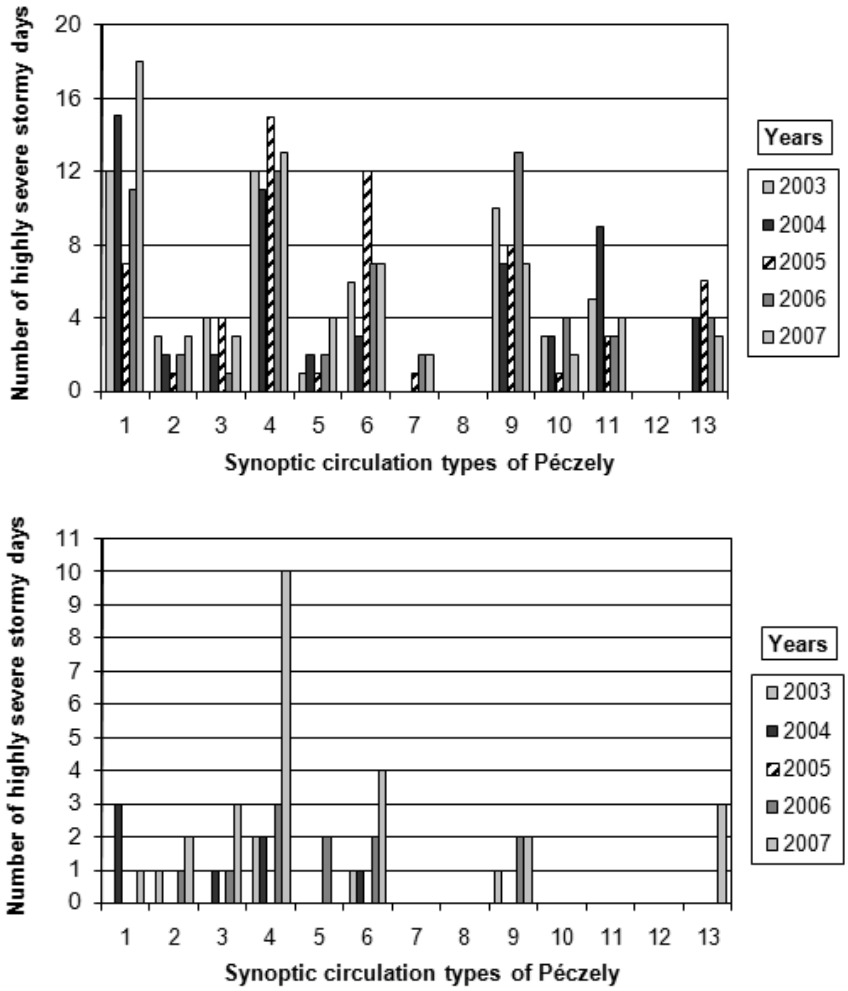


*Fig. 8.* Frequency distribution of highly severe stormy days with (up) few (the number of thunderstorm-ellipses does not exceed 50) and (down) many (thunderstorm-ellipses exceeds 50) thunderstorm-ellipses according to Péczely's synoptic circulation types in the years 2003, 2004, 2005, 2006, and 2007.

## *4. Conclusions*

This paper presents the results of an objective analysis which dealt with thunderstorm-climatology. The aims were to describe the space and time distribution of severe thunderstorms in Hungary and analyze the relationship between severe thunderstorms and synoptic circulation patterns for the five-year period 2003–2007.

The main results of the examination are as follows:

- The time distribution of stormy days was slightly different in each year. In 2004 and 2007 the stormiest days appeared in June, in 2003 and 2005 July had the stormiest days, while in 2006 August was the stormiest month. In the examined period, 2007 had the highest number of highly severe stormy days.
- Maxima of severe or highly severe thunderstorms/thunderstorm-ellipses were located in the south-western, in the northern central, and in the north-eastern parts of Hungary. The territory least at risk is the north-western region of the country.
- Most of the severe and highly severe stormy days and detected thunderstorms-ellipses are associated with various types of cold fronts and anticyclone-edges (Péczely-types 4, 1, 9, and 6 in order of frequency).
- The most dangerous situation of highly severe stormy days with many ellipses can be clearly linked to the type 4, which represents an open warm sector of an active cyclone.

In the future, this objective examination can be carried out for a longer period, since radar-measurements began in Hungary in the 1990s. Note that the radar measurements contain noise (and not all noise could be eliminated during this research), so in the near future a noise-filtering method should be developed.

***Acknowledgements***—The authors are grateful for the radar data provided by the Hungarian Meteorological Service. This research was supported by the Jedlik Ányos Program 2005, identification number: OM-00103/2005.

## *References*

*Adámy, L.* and *Máhr, J.,* 1963: Some statistical data of the thunderstorm climatology in Nyíregyháza and Szeged (in Hungarian). *Időjárás 67,* 226-232.

*Banta, R.M.* and *Schaaf, C.B.*, 1987: Thunderstorm genesis zones in the Colorado Rocky Mountains as determined by traceback of geosynchronous satellite images. *Mon. Weather Rev. 115*, 463-476.

*Bodolainé, J.E.* and *Tänczer, T.*, 2007: Mesoscale convective complexes. In *Atmospheric Convection* (in Hungarian) (ed.: *Á. Horváth*). Országos Meteorológiai Szolgálat, Budapest, 35-45.

*Braham, R.R.*, 1958: Cumulus cloud precipitation as revealed by radar-Arizona 1955. *J. Meteorol. 15*, 75-83.

*Brimelow, J.C., Reuter, W.G., Bellon, A.,* and *Hudak, D.,* 2004: A radar-based methodology for preparing a severe thunderstorm climatology in Central Alberta. *Atmos.-Ocean. 42,* 13-22.

*Craven, J.P.* and *Brooks, H.E.*, 2004: Baseline climatology of sounding derived parameters associated with deep, moist convection. *Nat. Wea. Digest 28,*13-24.

*Croft, P.J.* and *Shulman, M.D.,* 1989: A five-year radar climatology of convective precipitation for New Jersey. *Int. J. Climatol. 9*, 581-600.

*Dixon, M.* and *Wiener, G.*, 1993: TITAN: Thunderstorm Identification, Tracking, Analysis and Nowcasting – A radar-based methodology. *J. Atmos. Ocean. Tech. 10,* 785-797.

*Falconer, P.D.,* 1984: A radar-based climatology of thunderstorm days across New York State. *J. Appl. Meteorol. 23,* 1115-1120.

*Geerts, B*., 1997: Mesoscale convective systems in the Southeast United States during 1994–95: *A Survey Weather and Forecasting 13,* 860-869.

*Götz, G.* and *Pápainé, Sz.G.,* 1966: Thunderstorm activity in the summer-time period in Hungary (in Hungarian). *Időjárás 70,* 106-116.

*Götz, G.* and *Pápainé, Sz.G*., 1967: Thunderstorm activity in the winter-time period in Hungary (in Hungarian). *Időjárás 71,* 302-309.

*Héjas, E.,* 1898*: Thunderstorms in Hungary Based on Observations Between 1871 and 1895* (in Hungarian). Királyi Magyar Természet Tudományi Társulat, Budapest, 174 pp.

*Héjas, E.,* 1909: Space distribution of thunderstorms in Hungary (in Hungarian). *Földrajzi Közlemények 37,* 410-421.

*Henz, J.,* 1974: *Colorado High Plains Thunderstorm Systems - A Radar Synoptic Climatology.* Colorado St. Univ., M.S. Thesis, 82 pp.

*Horváth, Á.,* 2005: Synoptic description of the storm in May 18, 2005 (in Hungarian). *Légkör 50,* No. 3, 12-16.

*Horváth, Á.* and *Geresdi, I.,* 2000: Severe convective storms and associated phenomena in Hungary. *Atmos. Res. 56,* 127-146.

*Horváth, Á., Geresdi, I., Németh, P.*, and *Dombai, F.*, 2007: The Constitution Day storm in Budapest: Case study of the August 20, 2006 severe storm. *Időjárás 111,* 41-65.

*Időjárási Napijelentés* (*Daily Weather Reports*), 2003–2007: Országos Meteorológiai Szolgálat, Budapest.

*Jaeneke, M.*, 2001: Radar based climatological studies of the influence of orography on thunderstorm activity in Central Europe. *Proc. 30th International Conference on Radar Meteorology, 12A.5.*

*Kuo, J.* and *Orville, H. D.,* 1972: Radar climatology of summertime convective clouds in the Black Hills. *J. Appl. Meteorol. 12,* 359-368.

*MacKeen, P.L.* and *Zhang, J.,* 1999: Convective climatology for Central Arizona during the 1999 Monsoon (http://www.cimms.ou.edu/~heinsel/swconf.html).

*Manohar, K.* and *Kesarkar, A. P*., 2003: Climatology of thunderstorm activity over Indian Region: A study of east-west contrast. *Proc. ICAE Conference,* 121-124.

*Myers, J.,* 1964: Preliminary radar climatology of central Pennsylvania. *J. Appl. Meteor. 3*, 421-429.

*Ozorai, Z*., 1965: Thunderstorm frequency in Budapest-Ferihegy Airport (in Hungarian). *Időjárás 69*, 375-377.

*Paiva Pereira, L.G.* and *Rutledge, S.A.,* 2003: Convective characteristics over the East Pacific and Southwest Amazon regions: A radar perspective. *EPIC 2001 Workshop,* Boulder, CO, September 15-16, 2003.

*Péczely, G.* 1957: Grosswetterlagen in Ungarn. Kleinere Veröffentlichungen der Zentralanstalt für Meteorologie, Nr. 30, Budapest.

*Raum, O.,* 1910: Results of the 15-year thunderstorm observation in Hungary between 1896 and 1910 (in Hungarian). *Évkönyvek 40, 2*.

*Rigo, T.* and *Liasat, M.C.,* 2002: Analysis of convective structures that produce heavy rainfall events in Catalonia (NE of Spain), using meteorological radar. *Proc. ERAD*, 45-48.

*Schär, C., Lüthi, D., Beyerle, U.*, and *Heise, E.,* 1999: The soil-precipitation feedback: A process study with a regional climate model. *J. Climate 12,* 722-741.

*Shwehdi, M.H.,* 2005: Thunderstorm distribution and frequency in Saudi Arabia. *J. Geophys. Eng. 2,* 252-267.

*Steiner, M.* and *Houze, R.,* 1996: Sensitivity of the estimated monthly convective rain fraction to the choice of Z–R relation. *J. Appl. Meteorol. 36,* 452-462.

*Watson, A.I., Lopez, R.E.*, and *Holle, R.L.,* 1994: Diurnal cloud-to-ground lightning patterns in Arizona during the southwest monsoon. *Mon. Weather Rev. 122,* 1716-1725.

*Ziegler, C.L., Lee, J.T.*, and *Pielke Sr., R.A.,* 1997: Convective initiation at the dryline: A modeling study. *Mon. Weather Rev. 125,* 1001-1026.

# IDŐJÁRÁS

*Quarterly Journal of the Hungarian Meteorological Service*
*Vol. 112, No. 1, January–March 2008, pp. 15–31*


# Attempts to enhance the localization accuracy and to monitor the reliability of the SAFIR HMS lightning localization system


**Ferenc Dombai**

*Hungarian Meteorological Service*
*P.O. Box 38, H-1525 Budapest, Hungary; E-mail: dombai.f@met.hu*



*(Manuscript received in final form January 3, 2008)*



**Abstract—**In Hungary, an interferometric lightning localization network named SAFIR HMS was installed in 1998 to follow the total electrical activities of the thunderstorms for nowcasting purposes. In 2006 the real localization precision of SAFIR HMS was heavily investigated. In order to find the source of the gap between the promised and the experienced localization errors, different field measurements and simulation calculations were made. It was found that the random statistical errors of SAFIR HMS are about 0.5–1 degree, but the systematic localization errors could reach about 3–7 degrees in several directions from the detection stations. The badly compensated nonlinearities of the VHF detection sensors are the main sources of these systematic errors. It was found also, that the systematic localization errors could be reduced by reanalyzing of the raw detection data of the SAFIR HMS using the statistical differences of the measured (VHF interferometric) and calculated (from the positions of the return strokes with TOA method) azimuth data. In searching the way of the operational and automatic quality control of the SAFIR HMS, the Flash Backward Calculation (FBC) method have been developed at the Hungarian Meteorological Service (HMS). Using the raw detection data and the processed flash data, the FBC can continuously provide different detection activity and quality measures and detection errors of the SAFIR HMS, which can be fed later into automatic data assimilation processes.



*Key-words:* SAFIR, lightning localization, radar and lightning, localization error, localization accuracy, correction of localization error, reliability, Hungary


## *1. Introduction*

Many experienced problems and investigations have proved that the reliability and data quality of unmanned and embedded observation system are very critical. The importance of these is even more emphasized in using the so-called intensive observing systems to which the lightning localization system belongs.

Diversely from the conventional observing system, the information provided by intensive observing systems can not be easily proved in real-time, and detection errors can not be easily recognized because of the nature of data (*Dombai*, 2006). Lightning data are not continuous meteorological fields. The existence or the lack of such data depends on the real meteorological situation, but it depends on detection errors as well. The latter strongly depends on the technical reliability and the physical state of the observing system.

In 1998 an interferometric lightning localization network named SAFIR HMS was installed in Hungary to follow the total electrical activities of the thunderstorms with detecting and localizing the intracloud discharges on VHF and cloud to ground flashes on LF frequency bands. For long time period the localization precision of SAFIR HMS was far from the promised values. The evaluation of the real localization precision of SAFIR HMS was heavily investigated in 2006. In order to find the source of the gap between the promised and experienced localization errors, simulation calculations were done to evaluate the impacts of *random statistical* and *systematic* localization errors of the SAFIR HMS system. It was found that the badly compensated nonlinearities of detection sensors are the main sources of systematic localization errors, which could reach at about 3–7 degrees in some directions. The random statistical errors of SAFIR HMS are about 0.5–1 degree after our field measurements. It was found also, that the systematic localization errors could be reduced by reanalyzing the raw detection data of SAFIR HMS after having replaced measured azimuth data by corrected azimuth data calculated statistically after comparing the VHF interferometric return stroke positions and the LF TOA – time of arrivals – return stroke positions of the same flashes. The method of localization error calculations and reanalyzing of the SAFIR HMS raw data are described in Section 2.

In searching the way of the operational and automatic quality control of the SAFIR lightning localization system and the provided data, we have developed the *Flash Backward Calculation* method. Using the raw detection data on flashes arriving from detection station and the processed flash data calculated by the SAFIR CPS (Central Processing System), the FBC can continuously provide different activity and quality measurements, detection errors, etc., to be fed into the automatic processes of data assimilation. The method of FBC is described in Section 3.

## *2. Localization errors and reanalyzing of the SAFIR HMS data*

Since July 1998 the SAFIR HMS lightning localization system has been operated on national basis covering about 250,000 $km^2$ with 5 VHF/LF interferometric direction finder stations (*Dombai*, 1998). From 2000 the Hungarian Meteorological Service developed and introduced a forecaster's

workstation named HAWK for displaying different kinds of meteorological information in a unified coordinate system. The SAFIR HMS lightning data were also integrated into the HAWK display. From that time HAWK has become the unique displaying tool of lightning data for forecasters. The experiences gained by forecasters in the past years show that the SAFIR HMS data could be unreliable even for long time periods. In these periods, in spite of the fact, that the SAFIR status bars are green, the flashes displayed on HAWK are spatially very badly correlated with the radar or with the satellite data, and sometimes they have strange structures, sometimes not real flashes are displayed, and controversially, there are also severe thunderstorms without any flashes displayed. These cases make our forecasters uncertain, and they have very bad opinion about the reliability of the SAFIR HMS data. The joined display of flash data with radar and satellite data shows very sharply all kind of detection errors. By 2002 the SAFIR HMS was extended by the data of 2 additional sensors from Slovakia, which were giving more redundancy in the detection. In spite of this enhanced ability, the detection efficiency and technical reliability of SAFIR HMS were not enough improved (*Dombai*, 2004). As a consequence, the continuation of the functioning of the SAFIR HMS was seriously questioned in 2004. At this time, a special correction method was developed at the HMS to cut all flashes from the display, which are located outside of radar structures with values above dBZ – reflectivity thresholds (*Fülöp*, 2004) – to avoid the misinterpreting of meteorological situations and the false recognition of thunderstorms in the objective analyzing processes.

In 2005 three neighboring countries – Austria, Slovakia, and Hungary – with an extensive support of Vaisala (SAFIR system provider) started the FLASH cooperation aiming to have joined localization systems with more reliability and more precise localization capability on both VHF band – mainly cloud flashes and LF band – mainly return strokes (*Lojou*, 2005). After the evaluation of the first experiences gained on the course of the FLASH in 2005, two main issues were stated. Firstly, the SAFIR system has not enough tools for the continuous monitoring of the changes in the detection capabilities of sensors and all the system. It is typical that forecasters notify the system malfunctions with missed detection of flashes or situations with some extra detected flashes. Secondly, there is a big gap between the values of localization errors announced by the system providers (*Fig. 1*, left) and the localization errors experienced in the FLASH time period. Several times big localization errors around 10–20 km could be seen on HAWK comparing the flash cell positions to radar or satellite data (*Fig. 2*, right).

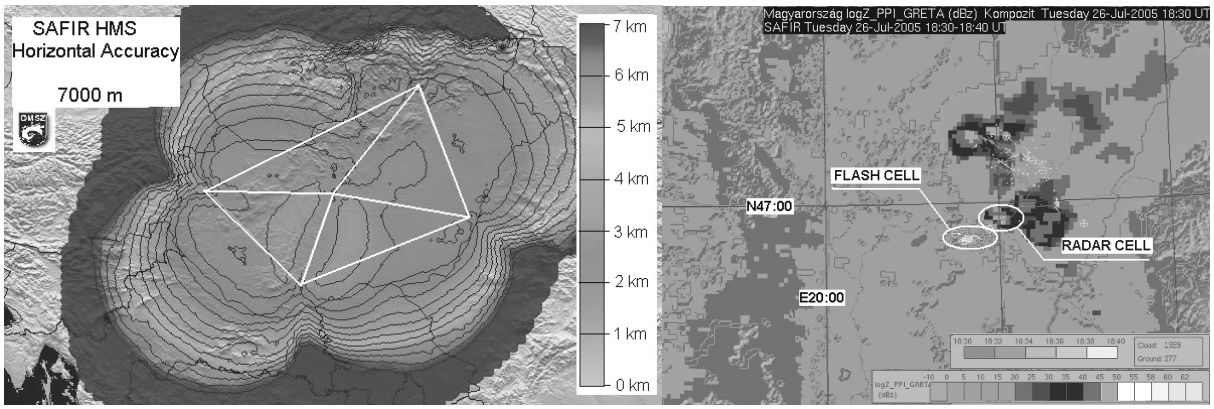


*Fig. 1.* Localization accuracy calculated by the Vaisala (left) and the localization errors frequently experienced on the HAWK (right – RADAR and SAFIR HMS data on July 26, 2005). The localization error is about 21–22 km.

## *2.1. Localization error calculations for the SAFIR HMS*

The SAFIR HMS is using the goniometric localization method, which means that the position of the VHF sources is determined by crossing points of lines originated from the stations and directed into the measured azimuths. A crossing point needs two lines from two stations. (In practice we have 5 stations, which are giving 10 pairs in result. The selection of appropriate pairs is part of the localization algorithms). The first step in the calculation of the localization error is the calculation of the localization error distribution of the station pairs. Considering the geometrical scheme of crossing lines in *Fig. 2* and the random statistical error of azimuth measurements we may assume, that the possible position of flash will be in the quadrilateral ($P_1$ $P_2$ $P_3$ $P_4$) which is determined by the crossing points of lines originated from stations into the azimuths modified with mean azimuth errors of stations. The mean error of the localization is assumed to be the square root of the area of this quadrilateral**.**

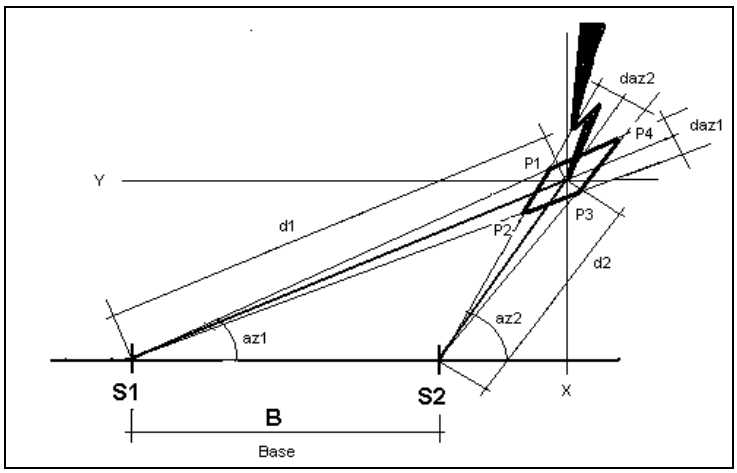


*Fig. 2.* Geometrical scheme for calculation of the localization error caused by inaccurate azimuth measurements by the SAFIR system.

In the calculation of the localization area we use the *Heron* equations for ($P_1$ $P_2$ $P_3$) triangulation to get the $A_1$ and for ($P_1$ $P_3$ $P_4$) triangulation to get the $A_2$ area values:

$$A_1 = \sqrt{s_1(s_1-a)(s_1-b)(s_1-c)} \quad \text{and} \quad A_2 = \sqrt{s_2(s_2-c)(s_2-d)(s_2-e)}, \qquad (1)$$

where

$$s_1 = 0.5(a+b+c) \quad \text{and} \quad s_2 = 0.5(c+d+e),$$

$$a = P_1\,P_2, \qquad b = P_2\,P_3, \qquad c = P_3\,P_1, \qquad d = P_3\,P_4, \qquad e = P_4\,P_1. \qquad (2)$$

The localization error will be

$$LE = \sqrt{A_1 + A_2}\,. \qquad (3)$$

To get the spatial distribution of localization errors, we need to calculate the localization area values for each grid point $P = (x, y)$ of the covered territory. For the numerical calculation of this we need to know *a, b, c, d, e* values, which are coming from the coordinates of the crossing points $P_1$, $P_2$, $P_3$, $P_4$. To get these coordinate values around each grid point, first we have to calculate the azimuth values of the lines originated from $S_1$ and $S_2$ stations to the crossing points $P_1$, $P_2$, $P_3$, $P_4$. To calculate these azimuths we need the azimuth of the grid points, which will be corrected with the azimuth errors $daz_1$, $daz_2$ later. The grid point azimuths, $t_1$ and $t_2$ will be:

$$t_1 = \text{atan}\,(m_1)\,57.3 \quad \text{and} \quad t_2 = \text{atan}\,(m_2)\,57.3, \qquad (4)$$

where

$$m_1 = (y - y_{S1}) / (x - x_{S1}) \quad \text{and} \quad m_2 = (y - y_{S2}) / (x - x_{S2}). \qquad (5)$$

The azimuths of the crossing points, $t_{11}$, $t_{12}$, $t_{21}$, and $t_{22}$, after correcting with azimuth errors $daz_1$ and $daz_2$ will be

$t_{11} = t_1 + daz_1/2$ and from $S_1$ to $P_1$ and $P_4$ $\quad t_{12} = t_1 - daz_1/2$ from $S_1$ to $P_2$ and $P_3$,

$t_{21} = t_2 + daz_2/2$ from $S_2$ to $P_1$ and $P_2$ and $t_{22} = t_2 - daz_2/2$ from $S_2$ to $P_3$ and $P_4$. (6)

Now these azimuth values have to be converted into the rise of curve values, $m_{ij}$ for calculating the crossing point coordinates:

$$m_{11} = \tan\,(t_{11}/57.3),\ m_{12} = \tan\,(t_{12}/57.3),\ m_{21} = \tan\,(t_{21}/57.3),\ m_{22} = \tan\,(t_{22}/57.3). \qquad (7)$$

Using these rises of curve values we get the coordinate values for crossing points $P_1(x_{11}, y_{11})$, $P_2\,(x_{21}, y_{21})$, $P_3(x_{22}, y_{22})$, $P_4\,(x_{12}, y_{12})$.

$$x_{11} = (m_{11}x_{S1} - m_{21}x_{S2} + y_{S2} - y_{S1})/(m_{11} - m_{21}) \text{ and } y_{11} = m_{11}(x_{11} - x_{S1}) + y_{S1} \text{ for } P_1,$$

$$x_{21} = (m_{12}x_{S1} - m_{21}x_{S2} + y_{S2} - y_{S1})/(m_{12} - m_{21}) \text{ and } y_{21} = m_{12}(x_{21} - x_{S1}) + y_{S1} \text{ for } P_2,$$

$$x_{22} = (m_{12}x_{S1} - m_{22}x_{S2} + y_{S2} - y_{S1})/(m_{12} - m_{22}) \text{ and } y_{22} = m_{12}(x_{22} - x_{S1}) + y_{S1} \text{ for } P_3,$$

$$x_{12} = (m_{11}x_{S1} - m_{22}x_{S2} + y_{S2} - y_{S1})/(m_{11} - m_{22}) \text{ and } y_{12} = m_{11}(x_{12} - x_{S1}) + y_{S1} \text{ for } P_4. \quad (8)$$

At last we get *a, b, c, d, e* values using the coordinate values from above:

$$a = \sqrt{(x_{11} - x_{21})^2 (y_{11} - y_{21})^2},$$
$$b = \sqrt{(x_{21} - x_{22})^2 (y_{21} - y_{22})^2},$$
$$c = \sqrt{(x_{22} - x_{11})^2 (y_{22} - y_{11})^2},$$
$$d = \sqrt{(x_{22} - x_{12})^2 (y_{22} - y_{12})^2},$$
$$e = \sqrt{(x_{11} - x_{12})^2 (y_{11} - y_{12})^2}. \quad (9)$$

In practice, to avoid the extreme localization errors caused by the very low azimuth differences between the crossing lines and by the large distances used in the localization algorithms, limitations are used for these parameters. *Fig. 3* shows the results of azimuth error calculations using the station pair with 160 km base line, and 1 and 2 azimuth errors. The minimum allowed azimuth difference was 10, and the maximum allowed distance was 260 km.

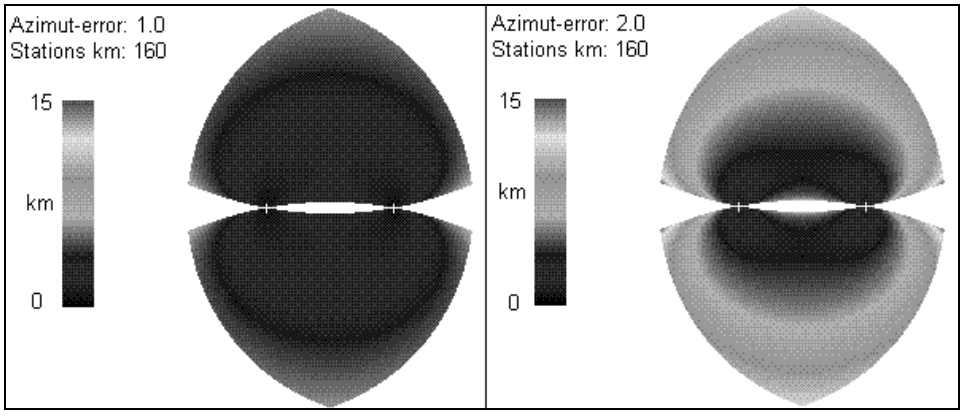


*Fig. 3.* Structures of localization accuracy of the station pair with 160 km baseline with azimuth errors 1.0° (left) and 2.0° (right). The maximum distance is 260 km and the minimum difference is 10° in azimuth from station1 and from station2.

In *Fig. 3* we can see that the promised localization accuracy of less than 5 km of the SAFIR HMS can be reached only if the azimuth errors are less than

1 degree at each station. If the azimuth errors are larger, the localization error will raise sharply up to 15 km or even more. By analyzing the localization errors calculated with different azimuth errors and baselines, we get that localization errors experienced on HAWK could be answered by supposing some 3–7 degrees variations of azimuth errors, which are far from the expected values.

In order to know the magnitude of the real values of azimuth errors and to evaluate the random statistical and the systematic part of these errors, several field measurements and analyses of raw detection data were done at the central station of the SAFIR HMS, Bugyi. The random statistical part of azimuth errors was evaluated by using fixed VHF sources and the systematic part by using azimuth differences between the detected azimuth by the SAFIR HMS and the calculated azimuth from the GPS coordinates of VHF sources. *Fig. 4* shows the results of field measurements.

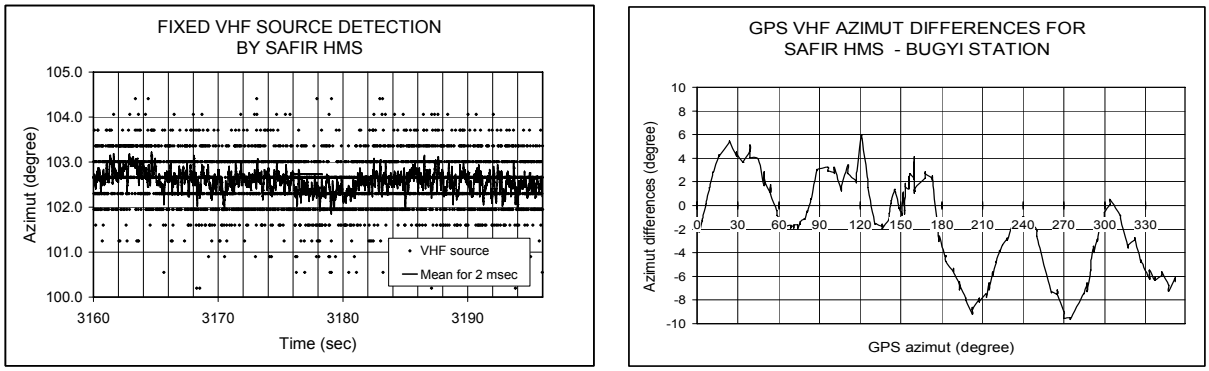


*Fig. 4.* Results of field measurements for azimuth errors of SAFIR HMS at Bugyi station. Left: random statistical errors – fix source measured on March 17, 2006, right: systematic errors – GPS-VHF azimuth differences around the station measured on June 22, 2006.

From *Fig. 4* left, we can see that the random statistical part of azimuth error is close to the promised values. In this case the dispersion is about 0.6 degree. But from *Fig. 4* right, we can see very large values for the systematic azimuth errors, which are varying from –8 to +5 degrees at Bugyi station. These values are in similar magnitudes to those found in the simulation calculations.

In the period of FLASH we have got a printed report from the Vaisala on the analysis of VHF performances of stations, which were made after the summer period of 2005 (*Lojou*, 2005). In this report VHF/LF coherence was calculated for return strokes using VHF interferometric azimuth and calculated azimuth from LF TOA (time of arrivals) positions. The TOA methods are not used in operational SAFIR 3000 systems, but these stations provide LF data with time resolutions suitable for TOA method. If we suppose that VHF and LF radiations of return strokes are coming from the same positions, then the azimuth values from LF TOA positions can be used as reference positions of VHF sources. Knowing the nature of real flashes it is rather strong hypothesis, but statistically it also seems to be proved. It needs more investigations, because

the TOA methods also have specific localization errors (*Hidayat* and *Ishii*, 1996). From this report we took the azimuth differences and calculated the difference curves shown in *Fig. 5* using spline interpolations. In *Fig. 5* we can see almost the same behavior of the systematic azimuth errors of SAFIR HMS as it was measured by us and shown in *Fig. 4*.

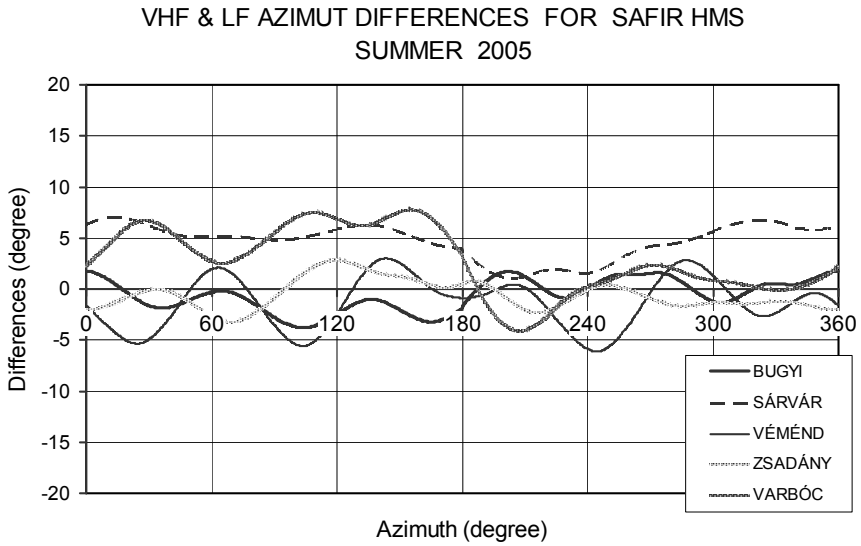


*Fig. 5*. Azimuth difference curves for all SAFIR HMS stations in the summer period of 2005. (The mean differences in the 0–360 azimuth are calculated between the interferometric VHF and the TOA LF positions of the same return strokes.)

The evaluation of the impact of the big systematic azimuth errors of stations is difficult and needs computer analysis. To do this we have developed a simulation program based on the method described in the previous section. We used the real geometry of the SAFIR HMS with all station pairs and triangulation parameters of localization, and we did azimuth corrections at each station with values of azimuth differences taken from the VAISALA report (*Lojou*, 2005). The calculations are going for each grid point of the covered territory with 2 km resolutions. The results of this simulation are shown in *Fig. 6*.

The localization errors were calculated with the so-called closer pair and mean methods. In the closer pair method a location point is calculated using azimuth values measured by stations, which are at minimum distance from the grid points. This method is used by the SAFIR HMS central processing. In this case the station pair indexes are calculated also marking the station pair providing the given location point. In the mean method a mean location point is calculated from all possible station pair azimuths. In this case a station pair number is calculated also, showing the number of pairs used for the mean position calculation.

*Fig. 6* shows that the closer pair method gives much bigger and more inhomogeneous localization error regions than the mean method. Very big

variances of this error changing from region to region can be seen on this maps, and there are very big jumps in these values in nearby regions, where the index of station pair determines the location point changes. In some regions the location error is almost zero, while in other regions these errors exceed 25 km. The inhomogeneous location error regions and these jumps give answer to the experienced phenomena of SAFIR HMS location problems. The deformed asymmetrical location error fields caused by the continuously changing systematic errors of stations in azimuth can be also seen on the location error maps.

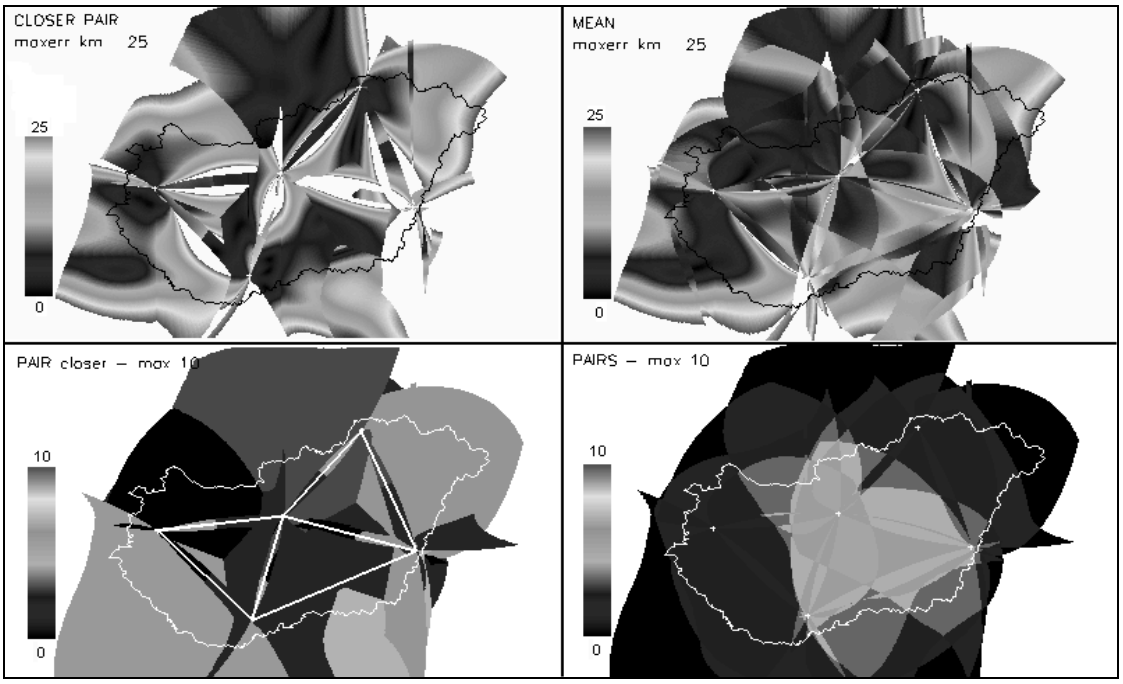


*Fig. 6.* Localization errors using the azimuth error curves of the SAFIR HMS stations. Closer pair – errors calculated with azimuths 'measured' by closer stations; pair – indexes of station pairs used in the closer pair calculation; mean – errors calculated with azimuths 'measured' by all of the stations; pairs – number of station pairs used in the mean calculations.

## *2.2. Correction of systematic azimuth errors and reanalyzing of the SAFIR HMS raw data*

The fact, that the systematic error can be considered constant in time, gives possibility to develop a method for compensating its impact on the localization data of SAFIR. We know that the correct solution is to create exact azimuth correction tables and load them into stations to compensate the site errors and the nonlinearity of phase measurements in real time processes. We have started to do this, but we have long time data series of lightning locations from which the impact of systematic location errors also needs to be filtered out. At the HMS we have developed a method for reanalyzing the time series of the SAFIR HMS raw data. For this reanalysis we used the two main type

of archived SAFIR data files. We used the so-called B$ archive files containing the VHF and LF detection data provided by the SAFIR stations and the so-called T$ archive files containing data on all localized intracloud flashes and return strokes.

The main steps of this reanalysis are the followings: By the analysis of B$ raw data files of SAFIR with DAM analyzing tool of Vaisala we can derive the azimuth difference curves of the VHF and LF locations. Using these curves we can calculate azimuth correction tables for each station, and using these correction tables we replace all the reported azimuth values by corrected ones in the raw SAFIR data files. At last the localization processes will be run again with the same triangulation but with modified north alignment values to provide us the corrected T$ localization data files. The impact of this reanalysis is illustrated in *Fig. 7*, which shows a map of the displacements of location points with directions and distances.

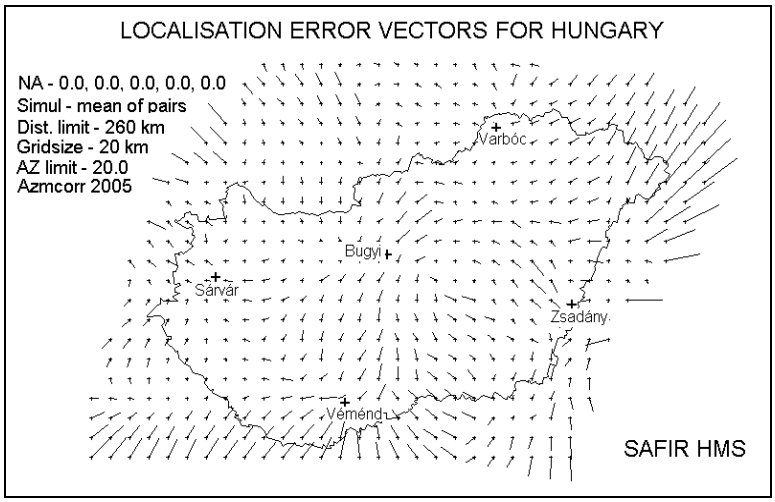


*Fig. 7.* Displacements of 'gridded flash positions'. Results of the simulation of the SAFIR HMS localization errors using azimuth differences on VHF and LF TOA of the SAFIR HMS stations.

For the validation of the reanalysis of SAFIR HMS data we have used jointly displayed radar and SAFIR HMS localization data precisely aligned in time and space. The time window for the SAFIR HMS data was +5 /–5 minutes around the time stamps of our national radar composites. The reanalysis has been done for the most severe thunderstorms in the summer period of 2005.

*Fig. 8* clearly shows that the reanalysis gives better correlated SAFIR HMS data with radar data. The flash cell structure has changed slightly and has been placed into the radar data covered regions near to the radar cells. This joint display after the reanalysis shows better correlated SAFIR HMS and radar data in general for the cases of 18 thunderstorm days of 2005. The reanalysis of the statistical characteristics of the azimuth differences also shows better localization accuracy (*Table 1*).

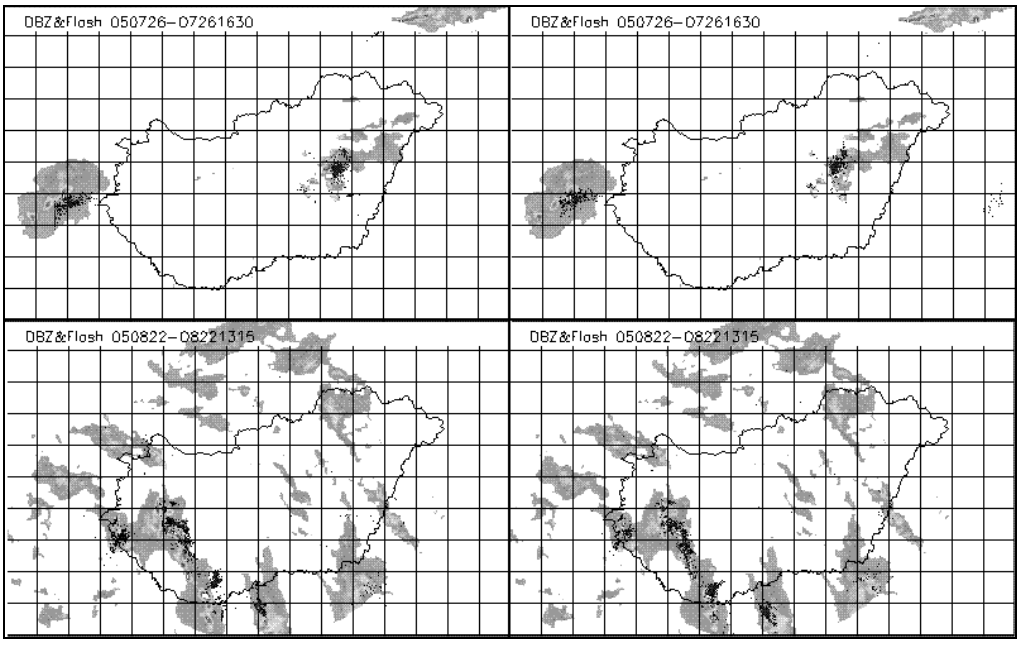


*Fig. 8.* Results of the reanalysis of SAFIR HMS data using azimuth differences curve of stations – jointly displayed SAFIR HMS location and radar reflectivity data on July 26, 2005 (above) and on August 22, 2005 (below). The original images are on the left, the reanalyzed ones are on the right. The grid size is 50 km.

*Table 1.* Statistical characteristics of the differences between VHF and LF TOA azimuths before and after reanalyzing the raw data of the SAFIR HMS in 2005

| | **Bugyi** | **Sárvár** | **Véménd** | **Zsadány** | **Varbóc** |
|---|---|---|---|---|---|
| **Before reanalyzing** | | | | | |
| Mean | -0.54 | 4.54 | -1.29 | -0.53 | 2.67 |
| Dispersion | 1.40 | 1.72 | 2.41 | 1.29 | 3.17 |
| Variances | 1.97 | 2.95 | 5.83 | 1.66 | 10.02 |
| Region | 4.92 | 6.33 | 8.79 | 5.63 | 11.60 |
| Minimum | -3.52 | 0.70 | -5.98 | -3.16 | -3.87 |
| Maximum | 1.41 | 7.03 | 2.81 | 2.46 | 7.73 |
| **After reanalyzing** | | | | | |
| Mean | -0.16 | 0.84 | -0.37 | -0.04 | 0.10 |
| Dispersion | 0.66 | 0.83 | 1.10 | 0.55 | 0.57 |
| Variances | 0.44 | 0.69 | 1.21 | 0.30 | 0.33 |
| Region | 3.16 | 3.52 | 4.57 | 2.81 | 2.46 |
| Minimum | -2.11 | -0.70 | -2.46 | -1.41 | -1.05 |
| Maximum | 1.05 | 2.81 | 2.11 | 1.41 | 1.41 |

The proposed correction method was applied for the correction of SAFIR HMS data on August 20, 2006. In the evening of this date, a very heavy thunderstorm was developed and moved through Hungary causing serious injuries and death at Budapest. Examining the jointly displayed radar and SAFIR HMS data on the HAWK system we noticed almost 50 km position errors in the southeast part of Hungary. After analyzing the azimuth differences

of VHF and LF TOA, we found very big azimuth errors for Zsadány station, which was caused by a big dephasing of a dipole pair (*Fig. 9*). After correcting the azimuth values of each VHF sources in the raw SAFIR HMS B$ file and making the processed T$ file with locations from the corrected B$, we reanalyzed the radar and SAFIR HMS data (*Fig. 10*).

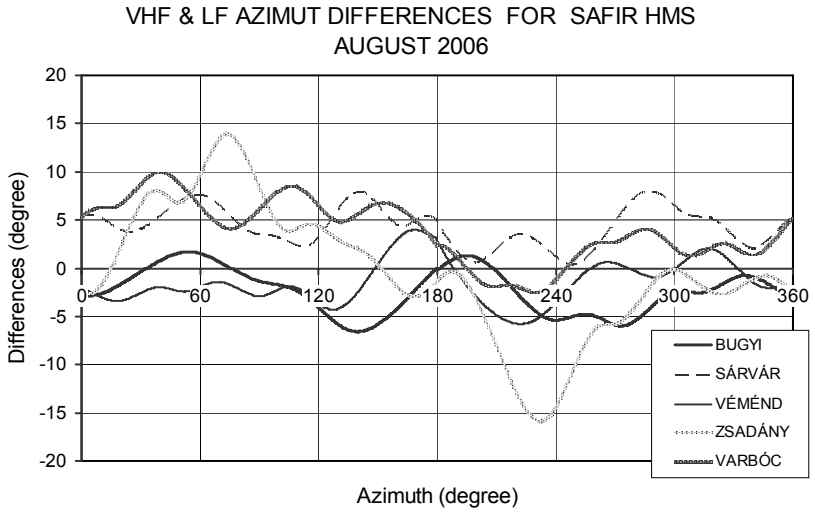


*Fig. 9.* Azimuth difference curves for all SAFIR HMS stations in August 2006. (The mean differences in the 0–360 azimuth were calculated between the interferometric VHF and the TOA LF positions of the same return strokes.) The azimuth error is very high for Zsadány station, it is about +/–15 degree.

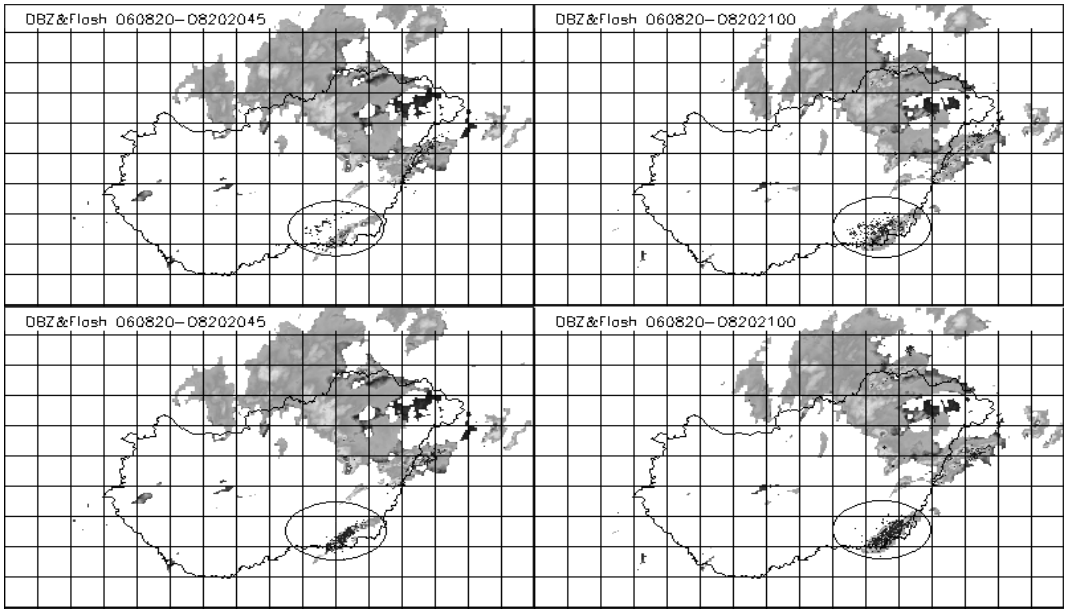


*Fig. 10.* Results of the reanalysis of SAFIR HMS data using azimuth differences curve of stations – jointly displayed SAFIR HMS location and radar reflectivity data on August 20, 2006, 20:45 UTC (left) and 21:00 UTC (right). The original images are above the reanalyzed ones are below. The grid size is 50 km. The corrected position error was about 50 km at the southeast part of Hungary.

Our correction method is a kind of site error correction method, although, in the focus of the developing was not the compensation of the site dependence of the propagation of the electromagnetic radiation of the flashes but the compensation of the systematic errors of the SAFIR HMS interferometric receivers.

## 3. *Flash backward calculation*

The basis of the FBC method is that from the data (time, geographical coordinates, amplitude, etc) of *localized flashes* we can derive all the set of the *detection data* (awaited detection time, azimuth, detection level, etc.), which most probably were detected at particular stations. After these calculations we match the calculated detection data with the real detected data for searching pairs between localized flashes and their real detection data at each station. When we have found the origins of localized flashes we mark the real detection data with MF and the calculated detection data with MD at each station. After this matching we can compare the *backwardly* calculated detection data with the *real* detected data for all flashes. In *Fig. 11* we illustrate this calculation method for the VHF sensors of SAFIR HMS.

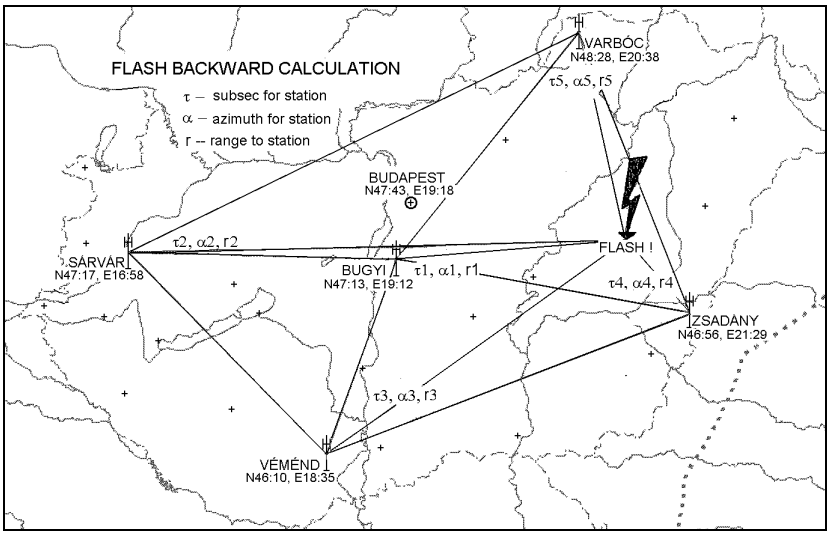


*Fig. 11.* Geographical positions of the SAFIR HMS stations, and the illustration of the FBC method.

In *Table 2* and *3* we illustrate the FBC results. The FBC was carried out on real flash data from T$ file and on real sensor data from B$ file for a thunderstorm on August 1, 1998. In these tables we show the successfully matched flashes and detections in a second time period. Columns of *Table 2* marked with MD indicate the ordering number of detections and vice versa columns of *Table 3* marked with MF indicate the ordering number of localized flashes.

*Table 2.* Flash data from T$ file and FBC data for each station with MD (matching number pointing for detections) on August 1, 1998 in the 53,443rd second time period of the day

| | Flashes | | | Hargita | | | | Sárvár | | | | Véménd | | | |
|---|---|---|---|---|---|---|---|---|---|---|---|---|---|---|---|
| **No.** | **subs.** | **x** | **y** | **subs.** | **azm.** | **dist.** | **MD** | **subs.** | **azm.** | **dist.** | **MD** | **subs.** | **azm.** | **dist.** | **MD** |
| 1 | 820 | 89.2 | 117.4 | 824 | 168 | 135.9 | 2 | 829 | 206 | 294.1 | 0 | 828 | 105 | 264.5 | 0 |
| 2 | 823 | 89.6 | 116.7 | 827 | 169 | 135.8 | 3 | 832 | 207 | 294.3 | 0 | 831 | 106 | 264.2 | 1 |
| 3 | 824 | 90.4 | 118.9 | 828 | 167 | 137.6 | 0 | 833 | 206 | 295.6 | 1 | 832 | 105 | 266.3 | 0 |
| 4 | 825 | 91.1 | 121.1 | 829 | 165 | 139.4 | 4 | 834 | 204 | 297.1 | 0 | 833 | 105 | 268.6 | 0 |
| 5 | 826 | 91.3 | 120.1 | 830 | 166 | 139.1 | 5 | 835 | 205 | 297.0 | 0 | 834 | 105 | 268.0 | 2 |
| 6 | 1477 | -0.3 | 114.4 | 1479 | 63 | 71.8 | 7 | 1483 | 188 | 209.1 | 0 | 1484 | 53 | 219.3 | 0 |
| 7 | 1478 | 2.1 | 116.3 | 1480 | 66 | 74.5 | 0 | 1485 | 187 | 212.1 | 0 | 1485 | 54 | 221.9 | 0 |
| 8 | 4017 | 9.4 | 129.8 | 4019 | 69 | 89.8 | 11 | 4024 | 180 | 224.4 | 0 | 4024 | 56 | 237.1 | 0 |
| 9 | 8169 | 66.7 | 243.3 | 8176 | 73 | 216.9 | 13 | 8180 | 143 | 335.0 | 0 | 8181 | 63 | 363.5 | 0 |
| 10 | 8997 | 71.2 | 248.1 | 9004 | 74 | 223.2 | 14 | 9008 | 142 | 341.6 | 2 | 9009 | 64 | 369.8 | 0 |
| 11 | 8998 | 71.4 | 245.4 | 9005 | 75 | 220.9 | 0 | 9009 | 144 | 340.0 | 0 | 9010 | 64 | 367.3 | 0 |
| 12 | 9027 | 9.7 | 139.6 | 9030 | 62 | 99.0 | 16 | 9034 | 174 | 229.2 | 0 | 9035 | 54 | 246.5 | 0 |

*Remarks for the columns:* subs – detection time in 100 us; x, y – coordinate of flashes in km; dist – distance to a flash from a station; MD – matching number pointing for a detection at a station

*Table 3.* Real sensor data from B$ file with MF (matching number pointing for flashes) on August 1, 1998 in the 53,443rd second time period of the day

| | Hargita | | | | Sárvár | | | | Véménd | | | |
|---|---|---|---|---|---|---|---|---|---|---|---|---|
| **No.** | **subs.** | **azm.** | **lev.** | **MF** | **subs.** | **azm.** | **lev.** | **MF** | **subs.** | **azm.** | **lev.** | **MF** |
| 1 | 812 | 153 | 101 | 0 | 834 | 182 | 80 | 3 | 832 | 98 | 77 | 2 |
| 2 | 824 | 161 | 95 | 1 | 9009 | 134 | 79 | 10 | 833 | 102 | 92 | 5 |
| 3 | 827 | 162 | 91 | 2 | 0 | 0 | 0 | 0 | 834 | 95 | 82 | 0 |
| 4 | 828 | 154 | 110 | 4 | 0 | 0 | 0 | 0 | 0 | 0 | 0 | 0 |
| 5 | 829 | 152 | 105 | 5 | 0 | 0 | 0 | 0 | 0 | 0 | 0 | 0 |
| 6 | 830 | 160 | 95 | 0 | 0 | 0 | 0 | 0 | 0 | 0 | 0 | 0 |
| 7 | 1479 | 40 | 101 | 6 | 0 | 0 | 0 | 0 | 0 | 0 | 0 | 0 |
| 8 | 1480 | 59 | 87 | 0 | 0 | 0 | 0 | 0 | 0 | 0 | 0 | 0 |
| 9 | 1956 | 31 | 84 | 0 | 0 | 0 | 0 | 0 | 0 | 0 | 0 | 0 |
| 10 | 2985 | 44 | 76 | 0 | 0 | 0 | 0 | 0 | 0 | 0 | 0 | 0 |
| 11 | 4020 | 54 | 82 | 8 | 0 | 0 | 0 | 0 | 0 | 0 | 0 | 0 |
| 12 | 4021 | 56 | 83 | 0 | 0 | 0 | 0 | 0 | 0 | 0 | 0 | 0 |
| 13 | 8176 | 64 | 77 | 9 | 0 | 0 | 0 | 0 | 0 | 0 | 0 | 0 |
| 14 | 9004 | 64 | 86 | 10 | 0 | 0 | 0 | 0 | 0 | 0 | 0 | 0 |
| 15 | 9005 | 69 | 92 | 0 | 0 | 0 | 0 | 0 | 0 | 0 | 0 | 0 |
| 16 | 9030 | 49 | 88 | 12 | 0 | 0 | 0 | 0 | 0 | 0 | 0 | 0 |

*Remarks for the columns*: subs – detection time in 100 us; azm – azimut of detected flashes; lev – signal level of detection; MF – matching number pointing for localized flashes

If MD or MF is equal to 0, it indicates that the matching was unsuccessful. When MD is equal to 0 at a station in *Table 2*, it means that the station did not detect that flash, *missed detection.* If MF is equal to 0 at a station in *Table 3*, it means that the station reports without flash, *false detection*. On the course of

FBC using the MD and MF marks we can calculate the differences between calculated and really detected parameters of flashes. Differences in azimuth and timing and relative amplitudes are illustrated in *Table 4*.

*Table 4.* Differences between the calculated and detected sensor data with MD (matching number) on August 1, 1998 in the 53,443rd second time period of the day

| | Flashes | | | Hargita | | | | Sárvár | | | | Véménd | | | |
|---|---|---|---|---|---|---|---|---|---|---|---|---|---|---|---|
| **No.** | **subs.** | **x** | **y** | **subs.** | **azm.** | **lev.** | **MD** | **subs.** | **azm.** | **lev.** | **MD** | **subs.** | **azm.** | **lev.** | **MD** |
| 1 | 820 | 89.2 | 117.4 | 0 | 7 | 0 | 2 | 0 | 0 | 0 | 0 | 0 | 0 | 0 | 0 |
| 2 | 823 | 89.6 | 116.7 | 0 | 7 | 0 | 3 | 0 | 0 | 0 | 0 | -1 | 8 | 0 | 1 |
| 3 | 824 | 90.4 | 118.9 | 0 | 0 | 0 | 0 | -1 | 24 | 0 | 1 | 0 | 0 | 0 | 0 |
| 4 | 825 | 91.1 | 121.1 | 1 | 11 | 0 | 4 | 0 | 0 | 0 | 0 | 0 | 0 | 0 | 0 |
| 5 | 826 | 91.3 | 120.1 | 1 | 14 | 0 | 5 | 0 | 0 | 0 | 0 | 1 | 3 | 0 | 2 |
| 7 | 1478 | 2.1 | 116.3 | 0 | 0 | 0 | 0 | 0 | 0 | 0 | 0 | 0 | 0 | 0 | 0 |
| 8 | 4017 | 9.4 | 129.8 | -1 | 15 | 0 | 11 | 0 | 0 | 0 | 0 | 0 | 0 | 0 | 0 |
| 9 | 8169 | 66.7 | 243.3 | 0 | 9 | 0 | 13 | 0 | 0 | 0 | 0 | 0 | 0 | 0 | 0 |
| 10 | 8997 | 71.2 | 248.1 | 0 | 10 | 0 | 14 | -1 | 8 | 0 | 2 | 0 | 0 | 0 | 0 |
| 12 | 9027 | 9.7 | 139.6 | 0 | 13 | 0 | 16 | 0 | 0 | 0 | 0 | 0 | 0 | 0 | 0 |

*Remarks for the columns:* subs – detection time in 100 us; x, y – coordinate of flashes in km; azm – azimut of detected flashes; lev – signal level of detection; MD – matching number pointing for detection at a station

The FBC method provides us not only the differences of measured and calculated detection parameters for all stations but also the possibility to set up different quality measurements and their ratings for each station or the whole system. The important derived parameters are the followings:

*Detection ratio* – detection number compared to the possible maximum VHF and LF,

*Good detection ratio* – proportion of detections associated with flashes at a station,

*False detection ratio* – proportion of detections without any flashes at a station,

*Missed detection ratio* – proportion of detections associated with flashes which are missing at a station,

*Good station* – stations where the *good detection ratio* is bigger than a threshold and the *false detection ratio* is smaller than a threshold,

*Azimuth error* – difference between detected and calculated azimuths on a flash.

In *Fig. 12* we can see a thunderstorm event on August 1, 1998. At the top, on the left the CC flash activity, on the right the station *VHF detection activities* are shown, at the bottom, on the left the *good detection ratio*, on the right the *false detection ratio* are shown for each station. We can see that two stations

were working with good detection ratio about 80% for all the time of the thunderstorm activity. For other stations this ratio was low, but the distances were high for those stations. When the false detection ratio is high it shows some detection level problems or noisy detection for those stations.

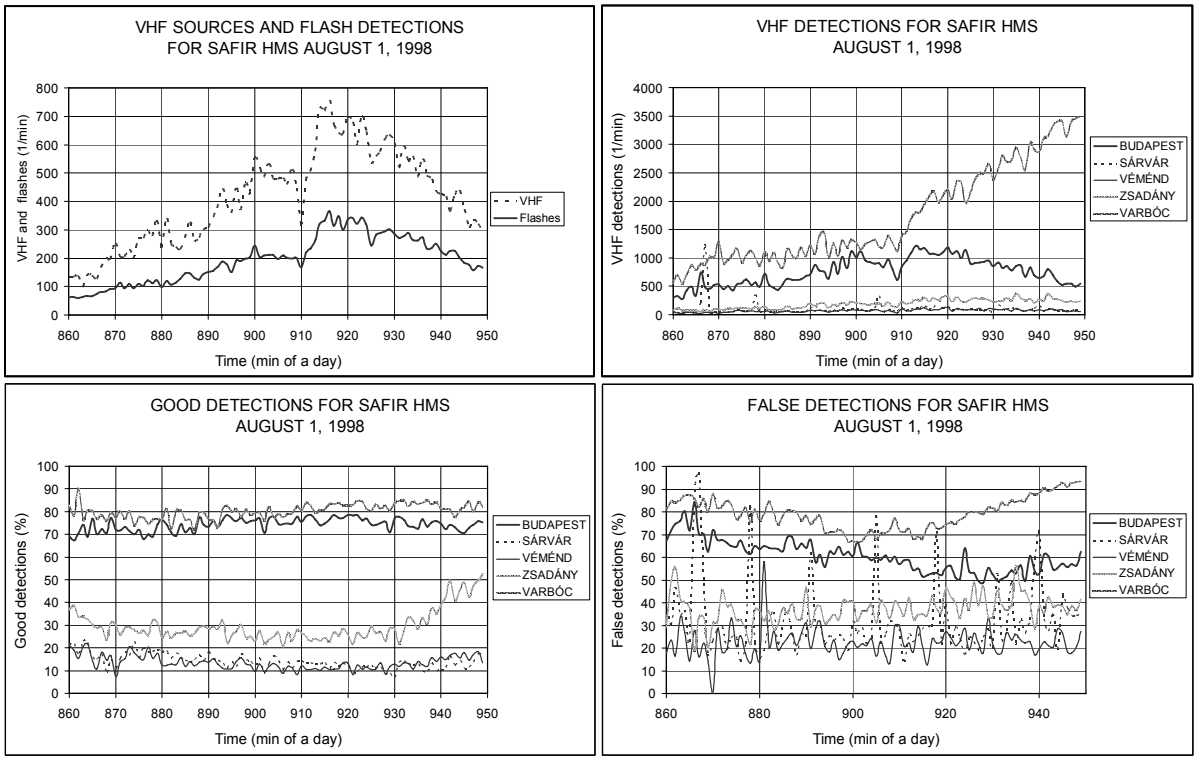


*Fig. 12.* Quality measurements from FBC results for a severe thunderstorm event on August 1, 1998.

The FBC can be done in real time and the results (azimuth errors, timing problems, detection level problems, etc.) could be displayed or sent to the maintenance team. Also the FBC can be equipped with *alarming levels* for different quality measurements, which could launch some automatic processes to avoid the long time system malfunctions. We hope that the results of our work will be implemented into operational practice soon.

## *4. Conclusions*

- The validation of the real localization accuracy is a very important question of the functioning of the SAFIR HMS system. Now this accuracy is far behind the promises, requirements, and possibilities.
- In this paper it was shown that the reanalysis of raw detection data with corrected azimuth data and the FBC calculation gives possibility to enhance the localization accuracy and reliability of the SAFIR HMS system.

- This reanalysis can help us only if the azimuth differences of VHF and LF TOA positions are derived from sufficiently long time series. The use of short time periods for such reanalysis needs more investigations. It is important, that during the reanalysis the significant changes and settings of station parameters (north alignment, Phi0 parameters, etc.) must be avoided.
- The results of the repeated coherence tests of the VHF and LF TOA azimuth on the corrected raw data files show that the azimuth differences decrease by a magnitude of 2, which means that the azimuth correction tables derived in this way are better to use than the azimuth correction tables provided by the SAFIR system providers.
- The best way to enhance the localization accuracy is to use station and site specific azimuth correction tables loaded into the stations. To get such tables, carefully made field measurements of azimuth responses of stations must be effectuated. We have further plans to carry out such measurements in the near future by using real time RTK GPS and a VHF signal generator.

## *References*


*Dombai, F.*, 1998: Lightning localization network in Hungary (in Hungarian). *Természet Világa (Special edition 1)*, 31–34.

*Dombai, F.*, 2004: On the reliability of the Hungarian SAFIR lightning localization network (in Hungarian). In *Meteorological Scientific Days – Intense Meteorological Observations* (ed.: *Gy. Gyuró* and *J. Nagy* ). Országos Meteorológiai Szolgálat, Budapest, 85–96.

*Dombai, F.*, 2006: The importance of advanced operational reliability and readiness monitoring of the SAFIR HMS lightning localization system. *Proceedings of the International Lightning Detection Conference.* Tucson, Arizona, 2006.

*Fülöp, A.*, 2004: Meteorological application of SAFIR lightning localization network data (in Hungarian). *Thesis of degree. Faculty of Meteorology at University of Eötvös Loránd*, Budapest.

*Hidayat, S.* and *Ishii, M.*, 1996: Error in lightning location by time difference and direction technique–Theory. *Transactions IEE Japan 116-B*, 410–416.

*Lojou, J.Y.*, 2005: Performance evaluation of the FLASH VHF sensors. *Flash Technical Report, Vaisala Inc., Tucson.*

*Richard, P.* and *Aufrray, G.*, 1985: VHF-UHF interferometric measurements, applications to lightning discharge mapping. *Radio Science 20*, 171–192.

# IDŐJÁRÁS

*Quarterly Journal of the Hungarian Meteorological Service*
*Vol. 112, No. 1, January–March 2008, pp. 33–43*


# Modeling water temperature of Hungarian rice fields


**Béla Gombos**

*Faculty of Agricultural Water and Environmental Management, Tessedik Sámuel College, Szabadság út 1-3, H-5540 Szarvas, Hungary; E-mail: gombos.bela@mvk.tsf.hu*



*(Manuscript received in final form February 15, 2008)*



**Abstract—**Low temperature during the sensitive phenophases of rice (*Oryza sativa* L.) can cause spikelet sterility. In Hungary this is one of the main weather and climatic risks resulting in yield loss. The thermal characteristics and heat balance of flooding water are very different from that of the air. Therefore, the modifying of water level gives an effective tool for rice growers to reduce cold stress. To help this and also to improve weather-rice models it is essential to predict water temperature from standard meteorological data.

Two empirical models were established based on water temperature measurements in a representative Hungarian rice field during the reproductive and early ripening stages from mid-July till the beginning of September in 2006 (model construction) and 2005 (model verification). Both models proved an efficient and accurate tool in simulating daily minimum, maximum, and average of flooding water temperature. The error in prediction is negligible from a practical point of view, especially if compared to the large differences between the extremes of air and water temperature.



*Key-words:* temperature, flooding water, rice (*Oryza sativa* L.), empirical model


## *1. Introduction*

Rice (*Oryza sativa* L.) is grown in Hungary on approximately 2000 hectares almost totally under flooded conditions. From the 3–4 leaf stages up to the dough ripening stage continuous water cover is ensured on the field (*Simonné*, 1983). This is the safest way to avoid sub-optimal water supply, which can reduce yield more for rice than for any other cereal crops (*Inthapan* and *Fukai*, 1988). Additionally, a water layer can act effectively in weed control and in thermal control of the fields. Rice growers working at high latitudes (Hungary, North Italy, North Japan, North China, South Australia) consider the water layer as the most important tool to reduce climatic risk caused by extreme temperature in the reproductive phenological phase (*Polgár*, 1961; *Wagner*, 1957; *Simonné*, 1979; *Confalonieri et al*., 2002; *Shimono et al*., 2005; *Gunawardena et al*.,

2001). As specific heat capacity of water is much higher than that of air, diurnal temperature amplitudes of flooding water are reduced (*Wagner*, 1966). In the night the flooding water is usually warmer than the air above it, and the benefit of deep water can reach 4 to 6 °C in Hungary (*Gombos*, 2007), 5 °C in Japan (*Shimono et al*., 2005) and 3.5 to 7 °C in Australia (*Gunawardena et al*., 2001). During the daytime temperature differences with an opposite sign are typical, which can be as high as 14 °C in some extreme situations (*Dingkuhn at al*., 1994).

Low temperature in the sensitive phenophases (booting stage, heading, anthesis) can result in significant yield loss due to spikelet sterility. The degree of damage is correlated more with water temperature (*Tw*) than with air temperature (*Ta*) (*Shimono et al*., 2005; *Roel et al*., 2005). The rate of development is also determined by water temperature until the growing point of rice is under the water level. Additionally, the temperature of flooding water plays an important role in temperature-dependent soil biochemical transformations. A micrometeorological model able to estimate *Tw* from *Ta* measured by standard meteorological stations (Stevenson screen) could significantly improve the accuracy and reliability of rice simulation models. More research is required to develop models of floodwater temperature and their incorporation into crop simulation models (*Confalonieri et al*., 2005, 2007; *Cola et al.*, 2007; *Mariani et al*., 2007). Studies of different kind of water masses provide some theoretical basis and practical information for modeling the effect of floodwater on microclimate of rice fields. However, adaptation of models is problematic, especially because of different vegetation (lack of vegetation, morpho-physiology of the plants), temporary, and spatial scales (*Burba et al*., 1999; *Jacobs et al*., 1997; *Gal et al*., 2003).

Two types of water temperature modeling approaches can be used, namely the deterministic (mechanical) and stochastic (statistical) approaches.

Empirical models based on reliable data can give a good prediction of water temperature, but their weakness is their limited validation. Such models can be used only under circumstances, which characterize the model parameterization. Mechanical models are more sophisticated and more general. They are based on physical equations (energy balance, turbulent transfer processes), but usually contain more or less empirical submodels.

In Hungarian rice fields the main determinants of floodwater temperature (i.e., meteorological conditions, canopy development and structure, irrigation water management) do not show large discrepancies. Therefore, an empirical model could be appropriate for the estimation of the water temperature of most rice fields. Our aim was to create such an empirical model, where the easy availability of input parameters is an important aspect, too.

The importance of such a floodwater temperature model is that it can be built in weather-rice models (simulation model, cold stress model) and be an effective tool for rice growers to calculate water temperature for the next 5–10 days using data of weather forecasts. This information can improve water management, particularly by highlighting the advantages of modifying the water level.

## 2. Materials and methods

### 2.1. Field measurements

Recently, Hungarian rice production has been concentrated in the south-eastern part of the country, predominantly in large farms in the Körös River Region. Therefore, a rice field of 200 hectares, approximately 1 km distance from the river Hármas-Körös (46°55'N, 20°32'E) was chosen as the study area. This territory is representative of the climatic, soil, and technological conditions of rice growing areas in Hungary. As is common, the field is subdivided into 4 ha ($200 \times 200$ m) units, where independent floodwater level management is possible. One of these plots with a stable and relatively high (25–30 cm) floodwater level with a well developed canopy of cultivar *Bioryza* supplied the basis for our measurements.

Temperature measurements were conducted in 2005 and 2006 from mid-July till the beginning of September during the reproductive and ripening stages of rice. Thermometers were placed near the centre of the plot to minimize the edge effect ("oasis-effect"). In 2005 mini waterproof thermologgers (HOBO Pendant UA-002) registered the water temperature at 5 and 15 cm and the soil temperature at 5 cm under the soil surface in every 20 minutes. In 2006, measurements were extended to the top water layer and to different levels of air. The water temperature at 25 cm and the air temperature at 35, 60, and 85 cm were measured with a thermologger with 4 external sensors (HOBO U12-006). The sampling interval was 5, 10, and 20 minutes in the air, water, and soil, respectively, according to their thermal characteristics.

Data on air temperature at 2 m were measured in a traditional weather shelter (Stevenson screen) at 1 km distance from the flooded rice fields (HOBO U12-006). Additionally, an automatic weather station (Vaisala MAWS-301) near the experiment area (4 km) supplied global radiation, wind, and humidity data.

A detailed data set from 2006 was used to construct the model, while verification was carried out with independent meteorological data from 2005.

### 2.2. The theoretical base and structure of the model

The energy balance of the water surface can be approximated as:

$$R_n + G + H + LE = 0, \tag{1}$$

where $R_n$ is the net radiation, $G$ is the heat stored in the floodwater and the subsoil, $LE$ is the latent heat flux, and $H$ is the sensible heat flux (*Oke*, 1978).

Heat stored in water ($G$) can be calculated from the change in mean water temperature:

$$G = c_w d \, \Delta Tw / \Delta t, \tag{2}$$

where ($\Delta Tw/\Delta t$) is the time rate of change in mean water temperature, $c_w$ is the water heat capacity, and $d$ is the water depth.

The flooding water temperature usually reaches its minimum ($Tw_{min}$) in the morning ($t_{min}$) and its maximum ($Tw_{max}$) in the late afternoon hours ($t_{max}$), i.e., $G > 0$ from $t_{min}$ till $t_{max}$ and $G < 0$ from $t_{max}$ till $t_{min}$ of the next day (*Wagner*, 1966; *Uchijima*, 1976; *Burba et al.*, 1999). These natural time intervals with non-identical length were chosen for the time steps of our model.

The total increase of heat stored in the floodwater during daytime ($G\uparrow$) is the integral of $G$ from $t_{min}$ to $t_{max}$, and the total decrease of heat during nighttime ($G\downarrow$) is the integral of $G$ (Eq. (2)) from $t_{max}$ to $t_{min}$ on the next day:

$$G\uparrow = c_w\, d\, \Delta Ti, \tag{3}$$

$$G\downarrow = c_w\, d\, \Delta Td, \tag{4}$$

where $\Delta Ti = Tw_{max} - Tw_{min}$, $\Delta Td = Tw_{min+1} - Tw_{max}$, and +1 in index means the next day.

The warming process during the daytime and cooling at night have different characteristics. During the daytime, the main driving force of energy balance is the incoming short wave radiation, and the temperature of flooding water decreases downwards from the surface resulting in stabile stratification (*Wagner*, 1966). At night, the long wave radiative cooling at the surface of the water body is the main driving force, and the decrease of water temperature in the top layer increases the water density, which is responsible for the growth of a mixing layer of uniform temperature and density.

A dynamic model was constructed, where daily $\Delta Ti$ and $\Delta Td$ values were empirically estimated and alternately cumulated during the whole study period. This process resulted in calculated time series of minimum and maximum water temperature values. It means, that natural time intervals with non-identical length – according to the sign of $G$ – were the time steps of our model.

The procedure of calculation is as follows:

1. estimating minimum water temperature of $Day_1$: giving an initial value of $Tw_{min,1}$,
2. calculating daytime increase of water temperature using an empirical relationship with meteorological parameters ($\rightarrow \Delta Ti_n$),
3. calculating maximum water temperature: $Tw_{max,n} = Tw_{min,n} + \Delta Ti_n$,
4. calculating nighttime decrease of $Tw$ using an empirical relationship ($\rightarrow \Delta Td_n$), and
5. calculating minimum water temperature: $Tw_{min,n+1} = Tw_{max,n} + \Delta Td_n$.

The value of $n$ represents the number of day of simulation ($n$ = 1: 1st day, $n = N$: final day). Steps from 2 to 5 are to repeat until $n = N$.

An initial water temperature value $Tw_{min,1}$ (or $Tw_{max,1}$) is needed, it have to be given in Step 1.

*2.3. Description of the empirical algorithm*

Our model estimates $\Delta Ti_n$ and $\Delta Td_n$ empirically. Only daily data available from standard meteorological stations were used in calculation of empirical relationships. In cases of both $\Delta Ti_n$ and $\Delta Td_n$, the water temperature was also used as input to ensure stability of the model due to negative feedback. To do this "warming force" (*WF*) and "cooling force" (*CF*) of the air were checked as possible input variables, as defined in Eqs. (5)–(6).

$$WF_n = Ta_{max,n} - Tw_{min,n}, \tag{5}$$

$$CF_n = Ta_{min,n+1} - Tw_{max,n}, \tag{6}$$

where $Ta_{max,n}$ is the daily maximum air temperature (°C) on $Day_n$ and $Ta_{min,n+1}$ is the daily minimum air temperature (°C) on $Day_{n+1}$. The physical basis of this assumption is that the sensible heat flux is a linear function of the temperature gradient. This means that the difference between the water and air temperature influences the heat storage term (*G*) and its integrals ($G\uparrow$ and $G\downarrow$). Consequently, *WF* and *CF* must be in a close linear relationship with $\Delta Ti$ and $\Delta Td$, respectively. Regression analyses showed that other air temperature parameters (such as average of different periods within a day) used in terms *WF* and *CF* can not improve the model significantly. Therefore, the best choice is to involve $Ta_{min}$ and $Ta_{max}$, especially because of the easy availability of these data.

The model construction was based on data set from July 20 until August 31, 2006. Water temperature in the medium water level was appropriate to use in model instead of the average temperature of the whole water layer (see details in Section 3)

Two models were constructed. Model 1 (M1) is a very simple one parameter linear regression with input parameters of only *WF* and *CF*, i.e., not more than the knowledge of daily maximum and minimum air temperature is required. Here $\Delta Ti$ and $\Delta Td$ are estimated using the regression equations (Eqs. (7)–(8)):

$$\Delta Ti = 0.323\ WF + 0.73, \tag{7}$$

$$\Delta Td = 0.387\ CF - 0.12. \tag{8}$$

Model 2 (M2) was developed by involving additional parameters into M1. The main criteria for each new input variable were:

- significant improvement ($P = 0.05$) of predicting power of regression,
- availability in standard meteorological data set,
- possibly low correlation with other model parameters,
- simplicity, with clear physical effect on water temperature.

Correlation analyses, stepwise (forward, interactive) regression analysis with Systat 9 statistical software, and applying the above criteria resulted in multilinear regression model:

$$\Delta Ti = 0.135\ RG + 0.133\ WF - 0.46, \tag{9}$$

$$\Delta Td = 0.282\ CF - 0.0473\ RH + 0.195\ w + 3.67, \tag{10}$$

where $RG$ is the daily sum of global radiation (MJ $m^{-2}$), $RH$ is the daily average of relative air humidity (%), and $w$ is the daily average wind speed (m $s^{-1}$) at 10 m height.

As expected, the increase of water temperature during daytime ($\Delta Ti$) was in strongest correlation with $RG$, but the temperature difference between air and water ($WF$) had similar importance.

$CF$ was the most important factor during the cooling period of water. $RH$ is in negative correlation with $\Delta Td$: in case of lower $RH$ values, latent heat loss from water becomes higher. Low $RH$ in daily average usually means strong radiation and higher air temperature at daytime, and so higher $\Delta Td$ values can occur because of the increased level of $Tw_{max}$, too.

Wind speed is not a significant factor in the daytime (Eq. (9)), but an important factor in cooling at night (Eq. (10)). Wind increases both sensible and latent heat fluxes, but in the daytime the direction of these fluxes is opposite. On the contrary, at night the direction of sensible and latent heat flux is usually identical, causing increased heat loss of water layer by windy weather.

### *2.4. Statistical analyses*

The daily water temperature values (mean, minimum, maximum) predicted by our model were compared with the measured values from the rice field. Four complementary statistical criteria were used to compare the predicted ($Tp_i$) and observed ($To_i$) values of daily temperature, $n$ being the number of day:

- Coefficient of determination ($CD$), which indicates whether the model reproduces the trend of measured values or not. Values near 1 are optimal.
- The root mean square error (RMSE):

$$RMSE = \sqrt{\sum \frac{(Tp_i - To_i)^2}{n}}. \tag{11}$$

  This calculation provides the mean difference between predicted and measured values, the smaller the $RMSE$, the better the prediction.
- The modeling efficiency ($EF$):

$$EF = 1 - \frac{\sum (Tp_i - To_i)^2}{\sum (To_i - \overline{To})^2}. \quad (12)$$

The optimum of this coefficient is 1; if positive, the model is a better predictor than the average of measured values.

- The coefficient of residual mass (*CRM*):

$$CRM = \frac{\sum To_i - \sum Tp_i}{\sum To_i}. \quad (13)$$

Positive coefficient values mean model underestimation, optimum value is 0.

## *3. Results*

The diurnal course of water temperature at different levels and the mean temperature of the whole floodwater layer – the average of August 2006 – is shown in *Fig. 1*. It can be clearly seen that at night (22–06 hours) the temperature is almost the same in each layer. In the evening the isotermia begins to develop first in the upper layer, and the mixed isotherm layer expands downwards. From the morning hours the incoming radiation builds up a well developed thermal gradient and stabile stratification of the flooding water. The mean temperature of the water body (calculated from values of the three levels) is close to the temperature of the medium water level (15 cm). The difference of their maximum values is only approximately 0.2 °C, and the minimum values are almost identical. Therefore, temperature of the medium level seems to be suitable to characterize the whole water layer.

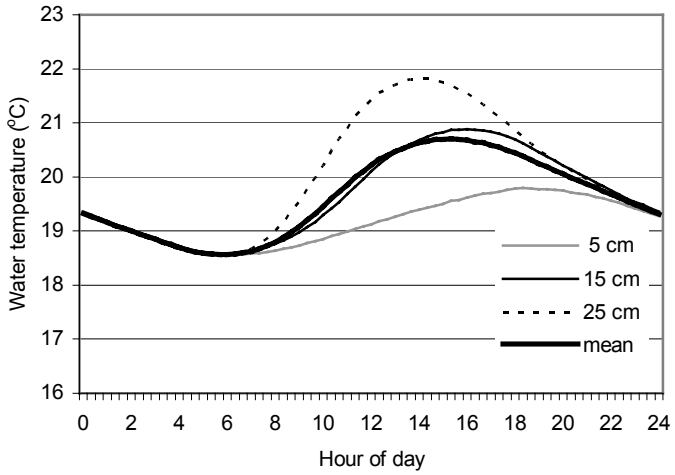


*Fig. 1.* Average diurnal course of the water temperature at different levels and mean temperature of the whole water layer in August 2006. (Height of the levels are given in centimeters above the soil surface.)

### *3.1. Model verification*

In our models the rates were calculated according to empirical relationships described in Eqs. (7)–(10). A parallel calculation of the rates was done to get the course of the minimum and maximum water temperature. Additionally, the averages of minimum and maximum were also determined and included in the verification as daily mean water temperature ($Tw_{mean}$).

A very good correspondence was found between the simulated and observed values in 2006, especially in case of Model 2 (*Fig. 2*). Model 1 (M1) accounted for 92% and 96% of the variation in minimum and maximum water temperature, respectively. Model 2 (M2) resulted in significantly better predictions than M1 with $CD$ = 0.98 both in $Tw_{min}$ and $Tw_{max}$. The *RMSE* values were reduced to nearly half due to the inclusion of additional input variables into M1 (*Table 1*). The model accuracy is evident in M2, looking at the low values of *RMSE*, at the values of EF close to one and of CRM very close to zero. Against the simplicity of M1, it also resulted in prediction with low error.

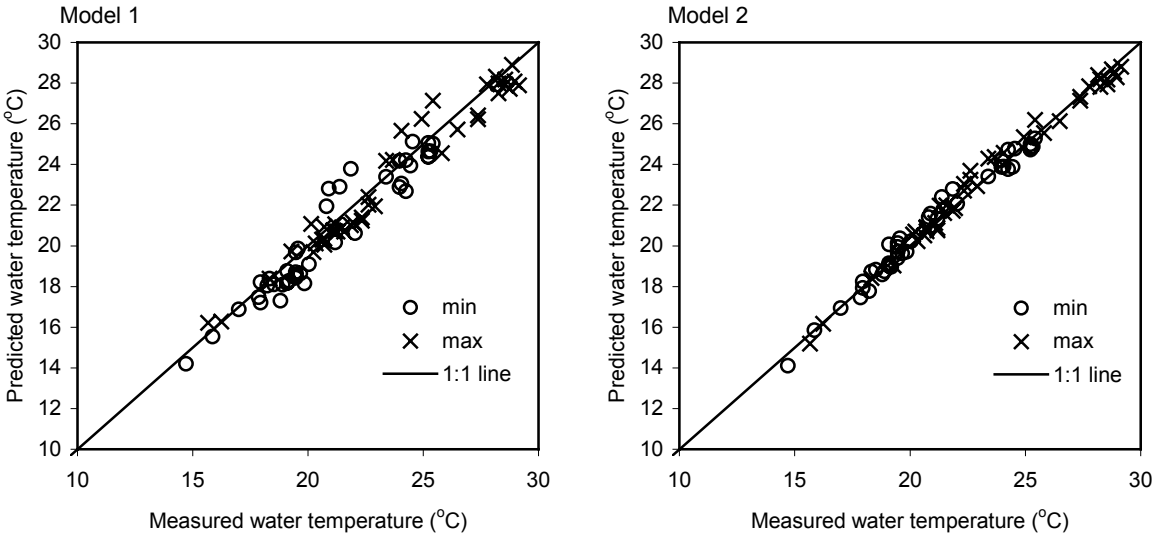


*Fig. 2.* Comparison of measured and predicted sets of water temperature (minimum, maximum) in 2006 (left: Model 1, right: Model 2).

In 2005, when the validation was based on independent data set, all of the fitting indices show that Model 2 has lost its advantage compared to Model 1. Moreover, in predicting $Tw_{min}$, M1 became slightly better than M2. Predicting $Tw_{max}$ is the weakest point of our models: *RMSE* = 1.31 (M1) and 1.2 (M2). Almost the same quality of information about mean water temperature is provided by M1 and M2. However, the statistical parameters proved the success of both models.

*Table 1.* Parameters of model verification

| | 2006 | | | | 2005 | | | |
|---|---|---|---|---|---|---|---|---|
| | ***RMSE*** | ***EF*** | ***CRM*** | ***CD*** | ***RMSE*** | ***EF*** | ***CRM*** | ***CD*** |
| **Model 1** | | | | | | | | |
| Min | 0.92 | 0.90 | 0.02 | 0.92 | 0.83 | 0.89 | 0.00 | 0.91 |
| Max | 0.78 | 0.95 | 0.01 | 0.96 | 1.31 | 0.81 | 0.01 | 0.83 |
| Mean | 0.79 | 0.94 | 0.01 | 0.95 | 0.93 | 0.87 | 0.01 | 0.89 |
| **Model 2** | | | | | | | | |
| Min | 0.44 | 0.98 | -0.00 | 0.98 | 1.01 | 0.84 | -0.03 | 0.89 |
| Max | 0.43 | 0.99 | -0.00 | 0.98 | 1.20 | 0.84 | -0.01 | 0.85 |
| Mean | 0.41 | 0.98 | -0.00 | 0.98 | 0.96 | 0.87 | -0.02 | 0.90 |

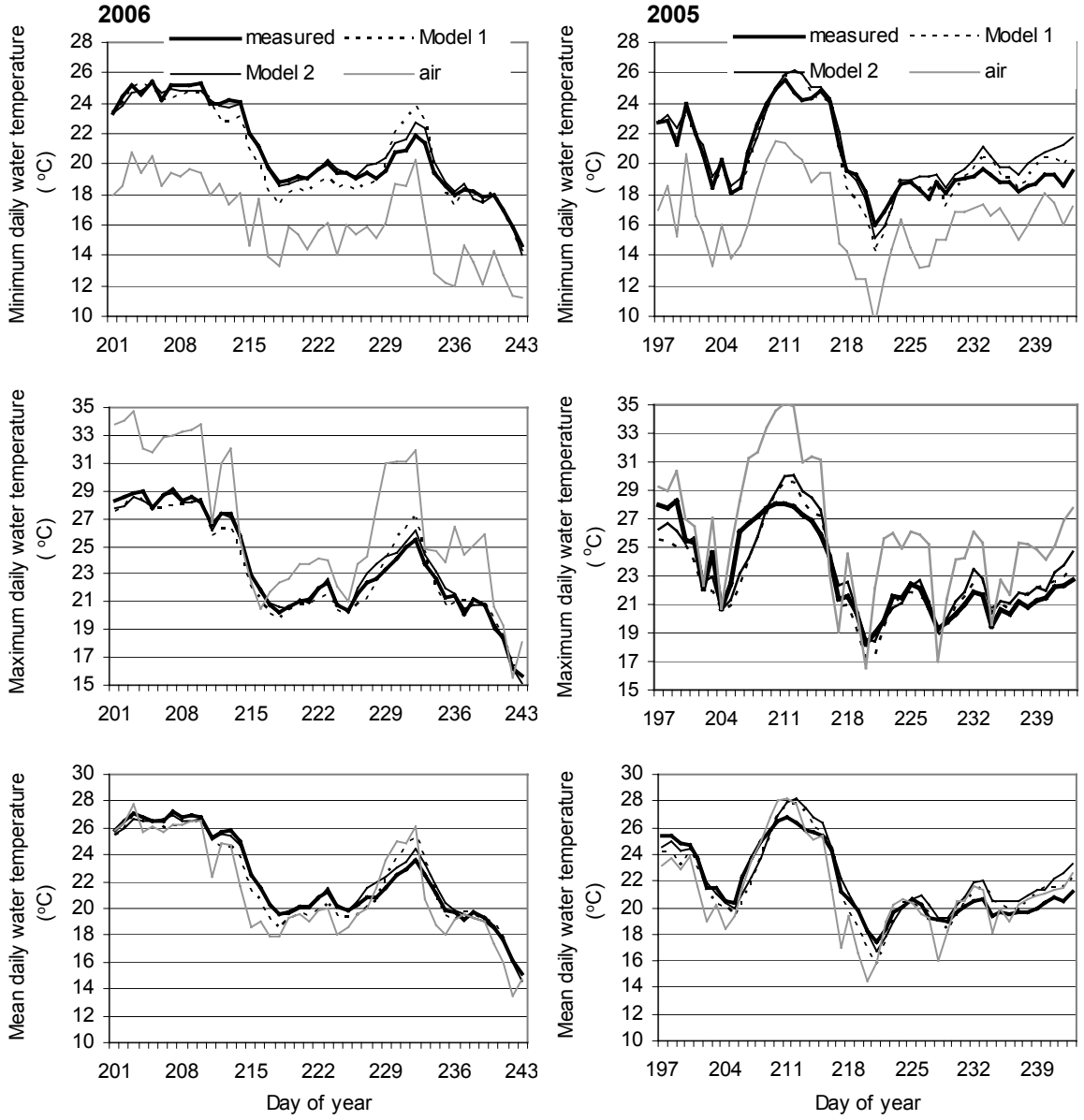


*Fig. 3.* Results of the modeling daily water temperature (minimum, maximum, mean). Prediction of Model 1 (dotted line) and Model 2 (solid line) compared with measured water (dark line) and air temperature (light line) in 2006 (calibration) and 2005 (verification).

*Fig. 3* clearly shows the improved ability of M2 in 2006 to predict the water temperature values ($Tw_{min}$, $Tw_{max}$, $Tw_{mean}$). M1 overestimated these water temperature parameters (especially $Tw_{min}$) by about 2 °C in the hot, sunny days after an intensive warming period (before August 20). It can be explained by clear, dry, and windy weather conditions, which were not handled properly by M1. The evaporation heat loss due to low *RH* and high windspeed was not captured in the model. A slight under-estimation of $Tw_{min}$ over a longer period can originate from an adverse effect.

In 2005 the highest predicting errors were recorded in $Tw_{max}$, during a hot, dry period, which occurred suddenly after cool days. The models showed a delayed reaction, then overestimation, similarly to the case in 2006 described above. The moderate warming period at the end of August 2005 (after DOY 235) was more critical for M2 than for M1. Global radiation, air humidity, and wind could not effect the water temperature as expected by Model 2. However, the mean water temperature was persistently lower than the mean air temperature hinting to circumstances different from typical case. It can be expected, that in such situations the more stable stratification of water with higher gradients in the top layer can cause errors in modeling.

## *4. Conclusions*

The thermal characteristics of rice flooding water are very different from that of the air. Therefore, estimating development rate, cold or heat stress, and yield of rice directly from air temperature data can lead to misleading results. Both of our empirical dynamic models proved an efficient and accurate tool in simulating water temperature. The error in prediction is neglible from a practical point of view, especially if compared to the large differences between extremes of air and water temperature. The very simple regression model (Model 1), which needs only daily maximum and minimum air temperature (from standard climate station) as input, is an easy tool for growers to use. It makes it possible to estimate the course of water temperature from the data of weather forecasts, and the results can directly help to make the right decisions for improved water management of paddy fields. The more sophisticated Model 2 provided very accurate predictions in 2006, but did not improve on Model 1 in the independent test period of 2005. Model 2 is recommended as a part of crop simulation models.

Our models in their present form are valid for a deep (20–30 cm) flooding water, and a well developed closed rice canopy under climatic conditions of Hungarian rice growing areas. In any other conditions (water depth, canopy, area), a new calibration of model is required.

# *References*


*Burba, G.G., Verma, S.B.,* and *Kim, J.*, 1999: Surface energy fluxes of *Phragmites australis* in a prairie wetland. *Agr. Forest Meteorol. 94*, 31-51.

*Cola, G., Bocchi, S.,* and *Mariani, L.*, 2007: Modelling of water temperature in flooded rice. *4th International Temperate Rice Conference*. June 25-28, 2007. Novara, Italy, 28-29.

*Confalonieri, R., Mariani, L.,* and *Bocchi, S.*, 2005: Analysis and modelling of water and near water temperatures in flooded rice (*Oryza sativa* L.). *Ecol. Model. 183*, 269-280.

*Confalonieri, R., Mariani, L., Facchetti, M.,* and *Bocchi, S.*, 2002: Analysis of temperature profiles in flooded rice field: Preliminary results. *Int. Rice Res. Notes 27*, 39-40.

*Confalonieri, R., Acutis, M., Donatelli, M., Genovese, G., Mariani, L., Gusberti, D., Trevisiol, P., Rodolfi, M., Picco, A.M., Cerrani, I.,* and *Bellocchi, G.*, 2007: WARM a new model for paddy rice simulations. *4th International Temperate Rice Conference.* June 25-28, 2007. Novara, Italy, 126-127.

*Dingkuhn, M., Sow, A., Samb, A., Diack, S.,* and *Asch, F.*, 1994: Climatic determinants of irrigated rice performance in the Sahel – I. Photothermal and micro-climatic responses of flowering. *Agr. Syst. 48*, 385-410.

*Gal, G., Imberger, J., Zohary, T., Antenucci, J., Anis, A.,* and *Rosenberg, T.*, 2003: Simulating the thermal dynamics of Lake Kinneret. *Ecol. Model. 162*, 69-86.

*Gombos, B.*, 2007: Study of water temperature in flooded rice (in Hungarian). *XIII. Ifjúsági Tudományos Fórum*. Pannon Egyetem Georgikon Mezőgazdaságtudományi Kar, Keszthely, 5 pp.

*Gunawardena, T.A., Fukai, S.,* and *Blamey, F.P.C.*, 2001: Nitrogen decreases deep irrigation efficacy in reducing low temperature damage in rice. In *Proc. of the 10th Australian Agronomy Conference.* Australian Society of Agronomy.

*Inthapan, P. and Fukai, S.*, 1988: Growth and yield of rice cultivars under sprinkler irrigation in south-eastern Queensland. 2. Comparison with maize and grain sorghum under wet and dry conditions. *Aust. J. Exp. Agr. 28*, 243-248.

*Jacobs, A.F.G., Jetten, T.H., Lucassen, D.C., Heusinkveld, B.G.,* and *Nieveen, J.P.*, 1997: Diurnal temperature fluctuations in a natural shallow water body. *Agr. Forest Meteorol. 88*, 269-277.

*Mariani, L., Donatelli, M., Confalonieri, R., Acutis, M.,* and *Cola, G.*, 2007: TRIS_DLL and TRIS_NET: two software components for simulating the floodwater effect on vertical thermal profile in paddy fields. *4th International Temperate Rice Conference*. June 25-28, 2007. Novara, Italy,128-129.

*Oke, T.R.*, 1978: *Boundary Layer Climates*. Methuen&Co., London, 370 pp.

*Petrasovits, I.*, 1958: Thermal effect of rice flooding water with different depth (in Hungarian). *Időjárás 62*, 95-107.

*Polgár, S.*, 1961: Water management of rice fields during cool down at late summertime (in Hungarian). *Debreceni Mezőgazdasági Akadémia Gyakorlati Szaktanácsadója 3*, 43-49.

*Roel, A., Mutters, R.J., Eckert, J.W.,* and *Plant, R.E.*, 2005: Effect of low water temperature on rice yield in California. *Agron. J. 97*, 943-948.

*Shimono, H., Hasegawa, T.,* and *Iwama, K.*, 2002: Response of growth and grain yield in paddy rice to cool water at different growth stages. *Field Crop. Res. 73*, 67-79.

*Shimono, H., Hasegawa, T., Moriyama, M., Fujimura, S.,* and *Nagata, T.*, 2005: Modeling spikelet sterility induced by low temperature in rice. *Agron J. 97*, 1524-1536.

*Simonné, K.I.*, 1979: *Problems of Hungarian Rice Production* (in Hungarian). MÉM Agroinform, Budapest, 36 pp.

*Simonné, K.I.*, 1983: *Rice Production* (in Hungarian). Mezőgazdasági Kiadó, Budapest, 293 pp.

*Uchijima, Z.*, 1976: Microclimate of the rice crop. In *Climate and Rice*. International Rice Research Institute, Manila, Philippines, 115-140.

*Wagner, R.*., 1957: Climatic data of rice fields in Kopáncs (in Hungarian). *Időjárás 61*, 266-277.

*Wagner, R.*, 1966: The temperature of soil, water and air in Kopáncs (in German). II. *Acta Climatologica VI.* 1-4, 1-51.

# IDŐJÁRÁS

*Quarterly Journal of the Hungarian Meteorological Service*
*Vol. 112, No. 1, January–March 2008, pp. 45–60*


# On the estimation of UV-B radiation over Egypt


**S. M. Robaa**

*Astronomy and Meteorology Department, Faculty of Science, Cairo University, P.O. Box 12613, Giza, Egypt; E-mail: d_robaa@hotmail.com*



*(Manuscript received in final form November 15, 2006)*



**Abstract—**In this study, four empirical formulae have been established and deduced to estimate UV-B radiation using sunshine duration, $n$, in cold and hot seasons at four stations that measure global and UV-B solar radiation in Egypt. Another empirical formula has been also deduced to estimate UV-B radiation in cold and hot seasons, at any locations in Egypt. The monthly mean UV-B values have been estimated at each station applying its own formula ($UVB$) and also applying Egypt's formula ($UVB_{eg}$). The estimated $UVB$ and $UVB_{eg}$ values were compared with the corresponding measured values at each station. The agreement between measured and estimated values is remarkable. The percentage errors of $UVB$ at each station, ($e_1$), were always found lower than the corresponding errors of $UVB_{eg}$, ($e_2$). It was found that the maximum possible error of estimated values does not exceed 8.0%. The annual mean values of $e_1$ ranged from – 0.6 to +3.1, while the annual mean values of $e_2$ ranged from –5.7 to +6.8. It is seen that the Egypt's formula gives precise estimations for UV-B radiation, and it is recommended for use at any locations in Egypt.

The UV-B radiation values have been estimated applying the Egypt's formula at forty selected stations to study the general distribution of UV-B over Egypt. The results revealed that the UV-B radiation depends on the latitude over Egypt. The maximum value of UV-B occurs in June in the southern part of Egypt and ranges from 0.080 to 0.088 MJ $m^{-2}$, while the minimum value occurs in January in the northern part of Egypt and ranges from 0.020 to 0.044 $m^{-2}$.



*Key-words:* global solar radiation, UV-B radiation, sunshine duration; estimation, Egypt


## *1. Introduction*

Ultraviolet solar radiation, UV, either at the edge of the atmosphere or at the earth's surface, accounts for only a small fraction of the total radiation flux. In the outer space, UV radiation accounts for only about 8.73% of the total solar radiation (*Al-Aruri et al*., 1988), while at any locations on the earth's surface, the UV radiation value depends on the solar zenith angle, atmospheric ozone content, and transparency of the atmosphere (*Kylling et al*., 2000; *Kirchhoff et*

*al.*, 2002; *Luccini et al.*, 2003). UV radiation wavelength range has been divided into three sub-ranges: UV-A (400–315 nm), UV-B (315–290 nm), and UV-C (290–220 nm). The mentioned lower limit of UV-C (220 nm) is valid only when it is studied in air, but in fact, the wavelength of the shortest wave ultraviolet beams is shorter than 100 nm. The earth's surface receives only UV-A and UV-B, while the UV-C component is removed not only by absorption through the protective ozone layer ($O_3$) but also because it provides energy for several photoionization processes. UV-B is partially absorbed by the ozone layer, while UV-A is transmitted (*McKenzie et al.*, 1995). The beneficial and damaging effects of UV-A and UV-B radiations on the humans, ecosystem, animals, plants, and materials are many (*Parrish et al.*, 1978; *Biswas*, 1979; *Giese*, 1982). High doses of ultraviolet radiation, especially band B, cause skin diseases, eye cataract, photo-decomposition, degradation of materials, and may also harm crops (*Som*, 1992). Inverse relation is known between the ozone concentration in the atmosphere and the amount of UV reaching the earth's surface. From this point of view, the UV radiation is highly affected by the ozone, which is destroyed by pollutants such as freon refrigerants, spray, and atomic bomb tests (*Elhadidy et al.*, 1990; *Feister* and *Grasnick*, 1992; *Tang et al.*, 1998; *Zerefos et al.*, 2001; *Wuttke et al.*, 2003; *Robaa*, 2005).

Although Egypt is a vast country, the number of its meteorological stations that measure the solar radiation components, especially UV-B radiation, is few (*Fig. 1*). Therefore, the main objective of this paper is to establish a simple model giving precise estimation for UV-B radiation at any locations in Egypt, where there are no measured data of solar radiation components or there are instrumental and other difficulties encountered in measuring components of solar radiation.

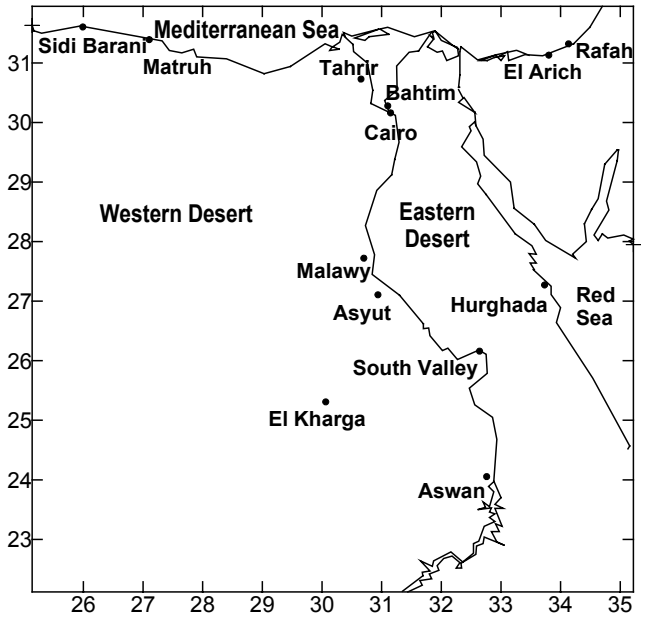


*Fig. 1*. Radiation network stations in Egypt.

## 2. Climate of Egypt

Egypt lies in north-east Africa. Most of Egypt's terrain is desert, divided into two unequal parts (eastern and western deserts) by the Nile River (*Fig. 1*). The valley and delta of the Nile are the main centers of habitation. The climate of Egypt is characterized by a hot season from March to September and a cold season from October to February. However, the northern winds are a welcome respite and do a good job of keeping the temperatures slightly moderated. The country is characterized by particularly good wind regimes with excellent sites along the Red Sea and Mediterranean coasts. Sites with an annual average of 8–10 m $s^{-1}$ have been identified along the Red Sea coast and about 6.0–6.5 m $s^{-1}$ along the Mediterranean coast. In the coastal regions, average annual temperatures vary from a maximum of 37 °C to a minimum of 14 °C. The most humid area is along the Mediterranean coast, where the average annual rainfall is about 200 mm. Rainfall decreases rapidly towards the south, and in many desert locations it may rain only once in several years. Temperatures vary widely in the inland desert areas, especially in summer, when it may range from 7 °C at night to 43 °C in daytime. During winter, temperatures in the desert fluctuate less dramatically, but they can be as low as 0 °C at night and as high as 18 °C in daytime. The average annual temperature increases moving southward from the Delta in the north to the Sudanese border in the south, where temperatures are similar to those of the open deserts. Throughout the Delta and the northern Nile Valley, there are occasional winter cold spells accompanied by light frost and even snow. In the south part of Egypt, June temperatures can be as low as 10 °C at night and as high as 41 °C in daytime, when the sky is clear. The entire territory enjoys a rather high solar radiation intensity of 1.9–2.6 kWh $m^{-2}$ $year^{-1}$. Further intensity up to about 2.4 kWh $m^{-2}$ $year^{-1}$ is observed when moving from the sea towards the desert.

A phenomenon of Egypt's climate is the hot spring wind that blows across the country. The winds, known to Europeans as the sirocco and to Egyptians as the khamsin, usually arrive in April, but occasionally occur in March and May. The winds form in small but vigorous low-pressure areas in the Isthmus of Suez and sweep across the northern coast of Africa. Unobstructed by geographical features, the winds reach high velocities and carry great quantities of sand and dust from the deserts. These sandstorms, often accompanied by winds of up to 40 m/s, can make temperature to rise as much as 20 °C in two hours. The winds blow intermittently and may continue for days, causing illness in people and animals, harm in crops, and occasionally damages in houses and infrastructure.

## 3. Measurements

The number of stations that measure the solar radiation components in Egypt is still few. Measurements of global solar radiation began in 1960 in Egypt at Tahrir station (see *Fig. 1* and *Table 1*). The ultraviolet radiation has been

measured in Egypt since 1990 at only two meteorological stations of Cairo in the north and Aswan in the south using an Eppley radiometer, which is sensitive to radiation in the wavelength band 290–385 nm (*Salem*, 2000; *Robaa*, 2005). Although, the study of UV-B radiation is very important for the various scientific purposes, it has been measured in Egypt at only four stations (*Fig. 1* and *Table 1*) using the UVB-1 ultraviolet pyranometer. The specifications of the UVB-1 pyranometer are given in *Table 2*.

*Table 1*. Coordinates of the Egyptian radiation network and the radiation components measured together with the date of commencement of recording

| Station | Lat. (N) | Long. (E) | Alt. (m) | Measurements | | | | | | Date of commencement of records |
|---|---|---|---|---|---|---|---|---|---|---|
| | | | | G | D | I | S | UV | UV-B | |
| Sidi-Barrani | 31.63 | 25.40 | 27 | M | M | - | M | - | - | 1984 |
| Matruh | 31.33 | 27.22 | 38 | M | M | - | M | - | - | 1961 |
| El-Arich | 31.08 | 33.82 | 32 | M | M | - | M | - | - | 1980 |
| Rafah | 31.22 | 34.20 | 73 | M | M | M | M | M | M | 1994 (2000) |
| Tahrir | 30.65 | 30.70 | 16 | M | M | - | M | - | - | 1960 |
| Bahtim | 30.13 | 31.25 | 17 | M | - | - | M | - | - | 1969 |
| Cairo | 30.08 | 31.28 | 36 | M | M | M | M | M | - | 1969 |
| Hurghada | 27.28 | 33.75 | 07 | M | M | - | M | - | M | 1990 (1994) |
| Malawy | 27.70 | 30.75 | 44 | M | M | - | - | - | - | 1994 |
| Asyut | 27.05 | 31.02 | 52 | M | - | - | M | - | - | 1979 |
| El-Kharga | 25.45 | 30.53 | 78 | M | M | - | M | - | - | 1964 |
| South Valley | 26.16 | 32.70 | 77 | M | M | - | M | M | M | 1994 (2000) |
| Aswan | 23.97 | 32.78 | 92 | M | M | M | M | M | M | 1972 (1998) |

The year in brackets indicates the date of commencement of UV-B radiation records. G is the global solar radiation, D is the diffuse solar radiation, I is the direct solar radiation, and S is the sunshine duration. M means existence of measurements.

*Table 2.* The operating characteristics of the UVB-1 pyranometer

| Characteristic | Description |
|---|---|
| Spectral response | 280 to 320 nm |
| Cosine response | ±5% for 0–60 degree solar zenith angle |
| Sensitivity | 1.97 W $m^{-2}$ $V^{-1}$ of total UV-B irradiance |
| Response time | approximately 0.1 second |

The first station is located within the premises of Rafah meteorological station on the extreme northeast boundary of Egypt. It lies in an open landscape of reclaimable desert, about 10 km to the south of the Mediterranean Sea coast. UV-B radiation measurements started at Rafah station in June 2000 and continued till now. The second station is located within the premises of Hurghada meteorological station, about 3 km to the west of the Red Sea coast and 5 kilometers to the north of the town. UV-B radiation measurements started at Hurghada station in January 1994 and continued only thirty three months to

finish in September 1996. The third station is located within the premises of South Valley meteorological station in south Egypt. The measurements of UV-B radiation started at South Valley station in April 2000 and continued till now. The last station is located in south Egypt within the premises of Aswan upper air station, to the west of the Aswan Dam. It is about two kilometers away from the high Dam Lake. UV-B radiation measurements started at Aswan station in August 1998 and continued till now (in addition to UV radiation measurements, which started in 1990). The measuring instruments are fixed on the roof of the building 7 m above the ground level at the four stations. The global solar radiation component is also measured at the above four stations using an Eppley precision spectral pyranometer (Model PSP). The accuracy of the pyaranometers corresponds to the first class according to the World Meteorological Organization classification (*WMO*, 1990). These instruments are calibrated each year against a reference instrument traceable to the World Radiometric Reference (WRR) maintained at Davos, Switzerland (see *WRC*, 1985, 1995). The absolute accuracy of calibration is ±3–4%, (*El-Metwally*, 2004). In the present work, daily values of global and UV-B solar radiation, that were measured through a three years period (2001–2003) at the stations of Rafah, South Valley, and Aswan, and through the period of January 1994–April 1996 at Hurghada station, have been obtained from EMA and used in this study. The monthly means have been calculated and also used in this study.

## *4. Results and discussion*

### *4.1. Methods of prediction*

*Sivkov* (1964) proposed the original empirical relation to estimate the monthly mean global solar radiation at the latitudes from 35º to 65ºN in the form:

$$G = 4.9(n)^{1.31} + 10550(\sin h)^{2.1}, \tag{1}$$

where $G$ and $n$ are the monthly global solar radiation (in cal cm$^{-2}$) and the monthly sunshine duration, respectively. $h$ is the solar elevation at noon on the 15th day of the month.

*Barbaro et al.* (1978) modified the above formula to fit 31 Italian stations that were divided into three zones according to their climatological characteristics. The modified formula is

$$G = K(n)^{1.24}(h)^{-0.19} + 10550\sin(h)^{2.1} + 300\sin(h)^{3}, \tag{2}$$

where $K$ = 8, 9.5, and 11 for zone 1, zone 2, and zone 3, respectively. The computation of $G$ is based on the knowledge of the appropriate zone parameter and long-term averages of sunshine duration and solar elevation.

Eq. (2), which was proposed for high latitudes (35º–65ºN), was tested by *Khogali* (1983) for low latitudes (4º–19ºN) and has been found applicable with a good degree of accuracy providing that the parameter *K* is appropriately adjusted.

Furthermore *Robaa* (2003) modified the empirical relation Eq. (2) to estimate global solar radiation in Egypt. In order to improve the obtained results, for prediction purposes, *Robaa* (2003) divided Egypt into five regions most representing the country. The regions are represented by the stations that measure solar radiation. *Table 1* gives a list of these stations and their coordinates in addition to the type of measured radiation at each station and the date of commencement of records. The year has been also divided into cold season (from October to February) and hot season (from March to September). *Robaa* (2003) determined an appropriate regional parameter, *K*, for the empirical relation Eq. (2) for each region during cold and hot seasons. He found that the modified formula gives precise estimations for global solar radiation at any Egyptian locations, whereas the percentage error was found ranging from –2.4 to +5.9 and having an annual mean value of 1.06 (*Robaa*, 2003). Therefore, the modified formula was recommended for use at any locations in Egypt to estimate the global solar radiation.

On the other hand, a significant correlation between *G* and *UV* radiation has been found by *Robaa* (2005) with a correlation coefficient of 0.98, and the standard error was close to zero. The recommended correlation equation has been stated to estimate the values of UV radiation, which can be measured with difficulty at the sites in the zone of Lower Egypt.

Although, the study of UV-B radiation is very important, as mentioned above, the measurements of UV-B radiation are not available at any locations in Egypt except of the four stations of Rafah, Hurghada, South Valley, and Aswan (*Fig. 1* and *Table 1*). Therefore, the main objective of this study is subjected to establish a simple model, which gives precise estimation for UV-B radiation at any Egyptian locations.

In this way, many types of correlations were tried to find out the best fit between the UV-B and global radiation at each station using all available daily measured values of the two parameters through the three years period (2001–2003) for Rafah, South Valley, and Aswan, and through the three years period (1994–1996) for Hurghada. On the other hand, all data of both UV-B and global radiations at the above four stations (3600 records for each parameter) have been used to find out the best fit between the two parameters for the whole territory of Egypt.

A significant positive correlation between the UV-B and global radiation has been found with correlation coefficients ranging between 0.9751 for the whole Egypt and 0.9816 for Aswan, and the standard errors were close to zero for the four stations and whole Egypt (see *Table 3*). The results are illustrated by *Figs. 2a-d* and they were found in the form:

$$UVB = aG + b, \tag{3}$$

where *a* and *b* are the regression coefficients which depend on the atmospheric conditions of the location. Data have been processed using an advanced computer program, and the calculated values of *a* and *b* for each station and the whole Egypt are given in *Table 3*, beside correlation coefficients, standard errors and the number of used records.

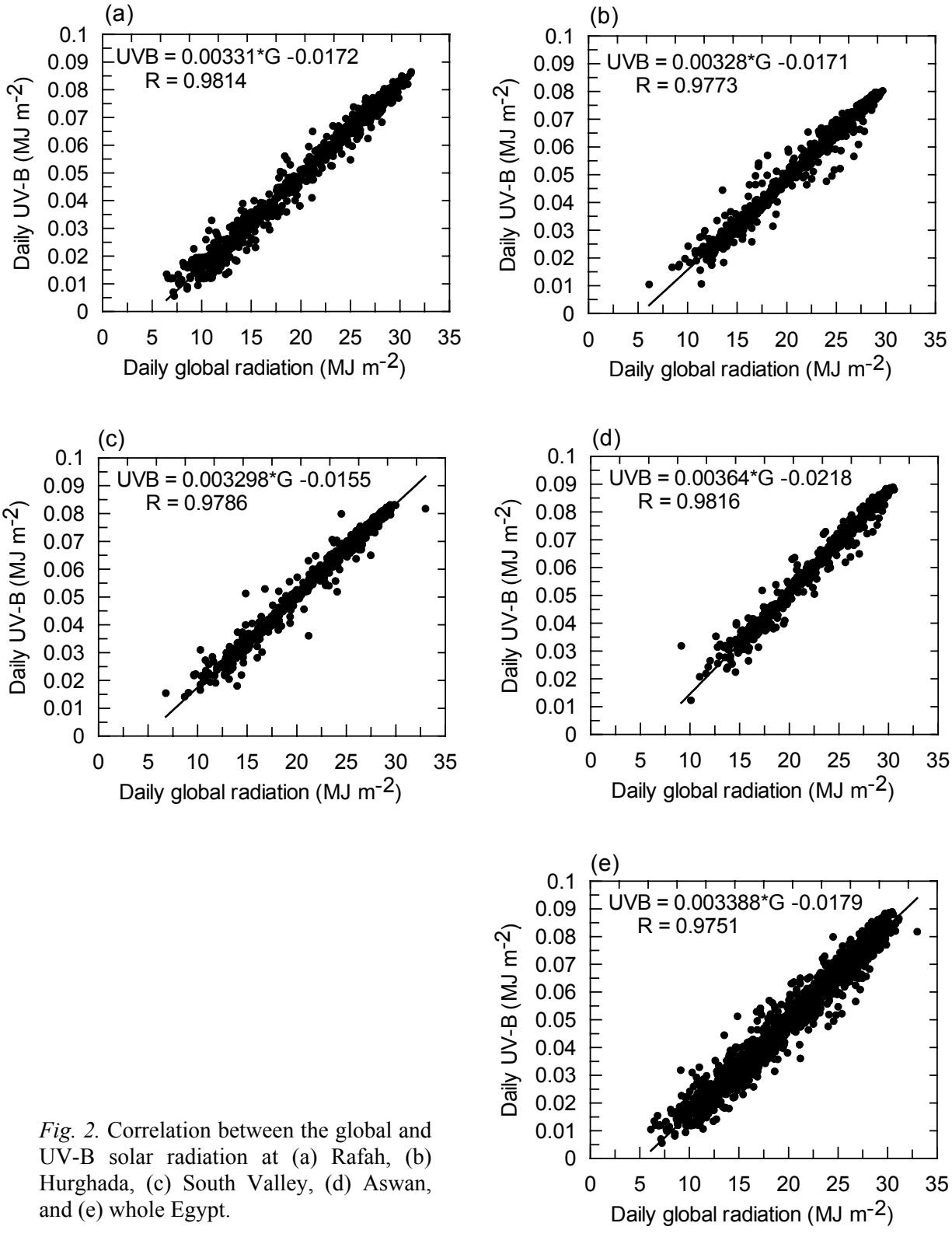


*Fig. 2.* Correlation between the global and UV-B solar radiation at (a) Rafah, (b) Hurghada, (c) South Valley, (d) Aswan, and (e) whole Egypt.

*Table 3.* The calculated values of regression coefficients, absolute error and the number of used records at the four stations

| Station | Regression coefficients | | Correlation coefficient | Standard error | Number of records |
|---|---|---|---|---|---|
| | *a* | *b* | | | |
| Rafah | 0.003307 | -0.017168 | 0.9814 | 0.00422 | 936 |
| Hurghada | 0.003283 | -0.017026 | 0.9773 | 0.00473 | 730 |
| South Valley | 0.003298 | -0.015453 | 0.9786 | 0.00398 | 993 |
| Aswan | 0.003641 | -0.021823 | 0.9816 | 0.00395 | 941 |
| Whole Egypt | 0.003388 | -0.017924 | 0.9751 | 0.02997 | 3600 |

From Eqs. (2) and (3) and Table (3), an empirical formula can be proposed to calculate *UVB* at the four stations and the whole Egypt during cold and hot seasons in the following form:

$$UVB = c_1 (n)^{1.24} (h)^{-0.19} + c_2 \sin(h)^{2.1} + c_3 \sin(h)^3 + b, \quad (4)$$

where $c_1 = a\,K$, $c_2 = 10550\,a$, and $c_3 = 300\,a$. The calculated values of $c_1$, $c_2$, $c_3$, and $b$ for each station and whole Egypt during cold and hot seasons are given in *Table 4*. The corresponding values of regional parameter $K$ for each station and whole Egypt have been taken from *Robaa* (2003) and given also in *Table 4*. $c_1$ values change from the cold to hot season at each station, while $c_2$, $c_3$, and $b$ take the same values during the two seasons at each station (see *Table 4*).

*Wang* and *Jianhui* (1996) stated that the impact of ozone depletion on UV radiation at the ground is greater on high latitudes than on middle and low latitudes. Furthermore, effect of the variability of ozone content is relatively low in Egypt (the difference between the highest and lowest monthly ozone values is 10.1% during the period of 1978–2004 (*Robaa* and *Hafez*, 2006)). Therefore, the ozone effect could be neglected in the used empirical formulae.

*Table 4.* Values of regional parameter $K$ and $c_1$, $c_2$, $c_3$ for each station and whole Egypt during cold and hot seasons

| Station | Season | $K$ | $c_1$ | $c_2$ | $c_3$ | $b$ |
|---|---|---|---|---|---|---|
| Rafah | Cold | 12.4 | 0.041007 | 34.88885 | 0.9921 | -0.017168 |
| | Hot | 14.6 | 0.048282 | | | |
| Hurghada | Cold | 11.5 | 0.037755 | 34.63565 | 0.9849 | -0.017026 |
| | Hot | 14.5 | 0.047604 | | | |
| South Valley | Cold | 14.3 | 0.047161 | 34.79390 | 0.9894 | -0.015453 |
| | Hot | 16.8 | 0.055406 | | | |
| Aswan | Cold | 13.5 | 0.049154 | 38.41255 | 1.0923 | -0.021823 |
| | Hot | 16.5 | 0.060077 | | | |
| Whole Egypt | Cold | 12.8 | 0.043366 | 35.74340 | 1.0164 | -0.017924 |
| | Hot | 15.5 | 0.052514 | | | |

An empirical formula can be easily deduced for each station and whole Egypt to calculate the monthly mean values of *UVB* during cold and hot seasons as follows:

*Rafah's formula:*

$$UVB = c_1 (n)^{1.24} (h)^{-0.19} + 34.88885 \sin(h)^{2.1} + 0.9921 \sin(h)^3 - 0.017168, \quad (5)$$

where $c_1$ value equals to 0.041007 and 0.048282 for cold and hot seasons, respectively.

*Hurghada's formula:*

$$UVB = c_1 (n)^{1.24} (h)^{-0.19} + 34.63565 \sin(h)^{2.1} + 0.9849 \sin(h)^3 - 0.017026, \quad (6)$$

where $c_1$ value equals to 0.037755 and 0.047604 for cold and hot seasons, respectively.

*South Valley's formula:*

$$UVB = c_1 (n)^{1.24} (h)^{-0.19} + 34.79390 \sin(h)^{2.1} + 0.9894 \sin(h)^3 - 0.015453, \quad (7)$$

where $c_1$ value equals to 0.047161 and 0.055406 for cold and hot seasons, respectively.

*Aswan's formula:*

$$UVB = c_1 (n)^{1.24} (h)^{-0.19} + 38.41255 \sin(h)^{2.1} + 1.0923 \sin(h)^3 - 0.021823, \quad (8)$$

where $c_1$ value equals to 0.049154 and 0.060077 for cold and hot seasons, respectively.

*Egypt's formula:*

$$UVB = c_1 (n)^{1.24} (h)^{-0.19} + 35.74340 \sin(h)^{2.1} + 1.0164 \sin(h)^3 - 0.017924, \quad (9)$$

where $c_1$ value to equals 0.043366 and 0.052514 for cold and hot seasons, respectively.

*4.2. Verification of the deduced empirical formulae*

To verify the deduced empirical formulae (Eqs. (5) to (9)), the monthly mean values of *UVB* have been calculated for Rafah, South Valley, and Aswan stations for the two subsequent years 2004 and 2005, and at Hurghada station for the two years of 1994 and 1995 in the cold and hot seasons. The calculated values have been produced for each station using the corresponding measured values of *n* and applying its deduced empirical formula to give *UVB* and the Egypt's formula (Eq. (9)) to give $UVB_{eg}$. The values of $UVB_{eg}$ have been calculated at each station to test the validity of the Egypt's formula for estimating *UVB* at any locations in Egypt.

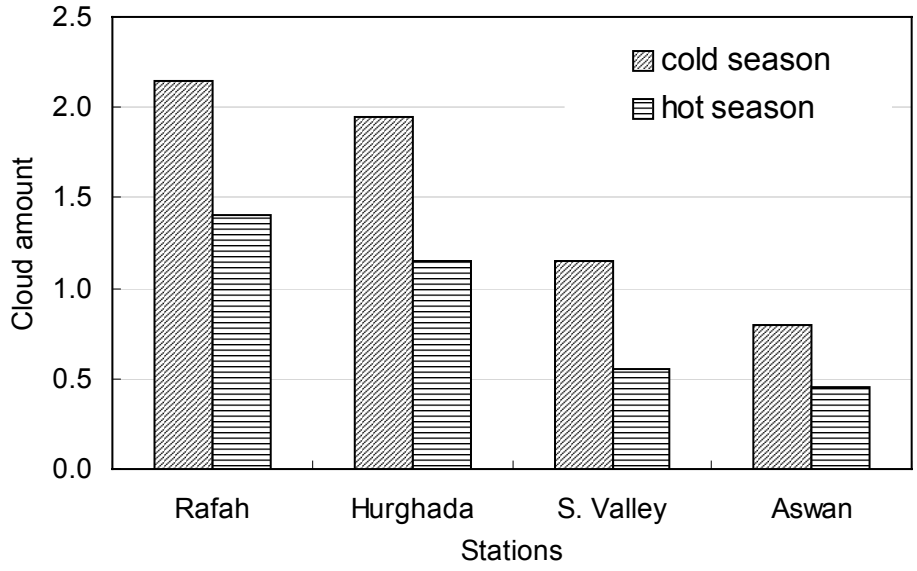


*Fig. 3.* Cloud amount (in octas) in the hot and cold seasons at the four studied stations (climatological normal value for the period 1975–2004).

The estimated *UVB* and $UVB_{eg}$ values at each station were compared with the corresponding measured values ($UVB_m$) during the same time period. The results are listed in *Tables 5* and *6*. It can be seen that the estimated values of *UVB* and $UVB_{eg}$ at each station are in a good agreement with the measured values for all months of the year. The percentage errors of *UVB* at each station, $e_1$, were always found lower than the corresponding errors of $UVB_{eg}$, $e_2$ (*Tables 5* and *6*). It was found that the percentage error, $e_1$, was ranged from –4.0 to +5.7 and from –3.3 to +4.9 during the two years, respectively, while $e_2$ was ranged from –7.5 to +8.0 and from –7.8 to +7.5 during the two years, respectively. The annual mean values of $e_1$ were ranged from –0.6 to +2.9 and from –0.3 to +3.1 during the two years, respectively, while the annual mean values of $e_2$ were ranged from –5.7 to +6.8 and from –5.4 to +5.8 during the two years, respectively (see *Table 7*).

It may be noted that the formula of each station gives precise estimation for UV-B radiation at its own locality with a small overestimation in the cold season (November to February) and underestimation in the remaining months. This is attributed to the higher effect of cloud cover (see *Fig. 3*) and atmospheric water vapor content in the cold season than in the hot and remain seasons. The cloud and atmospheric water vapor content effects are not taken in to the consideration with respect to the estimation formulae. On the other hand, it is to be noted that Eq. (9) of the whole Egypt overestimates the UV-$B_{eg}$ radiation all the year at Rafah and Hurghada, while underestimates it at South Valley and Aswan. This is because Rafah and Hurghada are coast cities and characterized by highest cloud cover (*Fig. 3*) and atmospheric water content during most of the year, especially in the winter season, while South Valley and Aswan are characterized by clear atmosphere and stable weather conditions.

*Table 5.* Sunshine duration $n$, solar elevation $h$, in addition to one year (2004) measured $UVB_m$ (MJ $m^{-2}$), estimated $UVB$ (applying the station's formula), and $UVB_{eg}$ (applying the Egypt's formula) values of the monthly mean UV-B radiation (MJ $m^{-2}$) and their percentage errors, $e_1$ and $e_2$

| Station | Parameter | Jan | Feb | Mar | Apr | May | Jun | Jul | Aug | Sep | Oct | Nov | Dec |
|---|---|---|---|---|---|---|---|---|---|---|---|---|---|
| **Rafah** | $n$ | 6.4 | 8.9 | 9.1 | 9.4 | 11 | 12.2 | 11.7 | 11.6 | 10.5 | 9.1 | 8.6 | 6.8 |
| | $h$ | 37.7 | 45.6 | 56.1 | 68.3 | 78 | 82.3 | 80.3 | 72.4 | 60.7 | 49 | 39.5 | 35.5 |
| | $UVB_m$ | 0.0201 | 0.0376 | 0.0518 | 0.0616 | 0.0712 | 0.0782 | 0.0742 | 0.0726 | 0.0618 | 0.0405 | 0.0309 | 0.0203 |
| | $UVB$ | 0.0203 | 0.0381 | 0.0501 | 0.0603 | 0.0703 | 0.0780 | 0.0741 | 0.0712 | 0.0606 | 0.0396 | 0.0309 | 0.0204 |
| | $UVB_{eg}$ | 0.0212 | 0.0397 | 0.0531 | 0.0636 | 0.0743 | 0.0824 | 0.0783 | 0.0754 | 0.0643 | 0.0412 | 0.0323 | 0.0213 |
| | $e_1$ | -1.2 | -1.4 | 3.4 | 2.1 | 1.2 | 0.3 | 0.1 | 2.0 | 1.9 | 2.2 | 0.0 | -0.3 |
| | $e_2$ | -5.4 | -5.5 | -2.5 | -3.3 | -4.3 | -5.4 | -5.5 | -3.8 | -4.1 | -1.9 | -4.5 | -4.7 |
| **Hurghada** | | | | | | | | | | | | | |
| | $n$ | 8.1 | 9.2 | 10 | 10.6 | 11.1 | 12.3 | 12 | 11.7 | 10.6 | 9.6 | 9 | 8.1 |
| | $h$ | 41.5 | 49.4 | 59.9 | 72.1 | 81.8 | 86.1 | 81.1 | 76.2 | 64.5 | 52.8 | 43.3 | 39.2 |
| | $UVB_m$ | 0.0290 | 0.0418 | 0.0572 | 0.0687 | 0.0716 | 0.0789 | 0.0764 | 0.0725 | 0.0647 | 0.0437 | 0.0346 | 0.0277 |
| | $UVB$ | 0.0278 | 0.0402 | 0.0562 | 0.0669 | 0.0709 | 0.0779 | 0.0748 | 0.0722 | 0.0628 | 0.0419 | 0.0330 | 0.0261 |
| | $UVB_{eg}$ | 0.0312 | 0.0443 | 0.0603 | 0.0714 | 0.0756 | 0.0832 | 0.0800 | 0.0773 | 0.0673 | 0.0463 | 0.0369 | 0.0295 |
| | $e_1$ | 4.1 | 3.9 | 1.7 | 2.6 | 1.0 | 1.2 | 2.1 | 0.4 | 2.9 | 4.0 | 4.5 | 5.7 |
| | $e_2$ | -7.5 | -5.9 | -5.4 | -3.9 | -5.6 | -5.5 | -4.7 | -6.6 | -4.0 | -6.0 | -6.8 | -6.4 |
| **South Valley** | | | | | | | | | | | | | |
| | $n$ | 9.5 | 9.9 | 10.2 | 10.7 | 11.2 | 12.4 | 12.2 | 11.8 | 10.7 | 9.8 | 9.1 | 8.4 |
| | $h$ | 42.6 | 50.6 | 61 | 73.3 | 82.9 | 87.2 | 82 | 77.3 | 65.7 | 53.9 | 44.5 | 40.5 |
| | $UVB_m$ | 0.0401 | 0.0499 | 0.065 | 0.0772 | 0.081 | 0.088 | 0.0812 | 0.08 | 0.0719 | 0.0507 | 0.0398 | 0.0331 |
| | $UVB$ | 0.0409 | 0.0507 | 0.0650 | 0.0751 | 0.0790 | 0.0866 | 0.0840 | 0.0810 | 0.0714 | 0.0505 | 0.0410 | 0.0344 |
| | $UVB_{eg}$ | 0.0381 | 0.0482 | 0.0621 | 0.0724 | 0.0763 | 0.0837 | 0.0811 | 0.0781 | 0.0685 | 0.0480 | 0.0383 | 0.0317 |
| | $e_1$ | -1.9 | -1.6 | 0.0 | 2.7 | 2.5 | 1.6 | -3.5 | -1.2 | 0.7 | 0.4 | -2.9 | -4.0 |
| | $e_2$ | 5.0 | 3.4 | 4.5 | 6.2 | 5.8 | 4.8 | 0.1 | 2.4 | 4.7 | 5.4 | 3.7 | 4.1 |
| **Aswan** | | | | | | | | | | | | | |
| | $n$ | 10 | 10.2 | 10.4 | 10.8 | 11.5 | 12.6 | 12.4 | 12 | 10.8 | 10 | 9.2 | 9 |
| | $h$ | 44.3 | 52.5 | 63 | 75 | 83.8 | 87.8 | 83.8 | 78.7 | 68.9 | 57.6 | 47.6 | 42.6 |
| | $UVB_m$ | 0.0440 | 0.0542 | 0.0695 | 0.0796 | 0.0844 | 0.0920 | 0.0894 | 0.0864 | 0.0767 | 0.0554 | 0.0433 | 0.0375 |
| | $UVB$ | 0.0442 | 0.0544 | 0.0695 | 0.0795 | 0.0842 | 0.0919 | 0.0894 | 0.0862 | 0.0765 | 0.0548 | 0.0436 | 0.0379 |
| | $UVB_{eg}$ | 0.0416 | 0.0511 | 0.0643 | 0.0736 | 0.0779 | 0.0847 | 0.0823 | 0.0795 | 0.0708 | 0.0516 | 0.0412 | 0.0359 |
| | $e_1$ | -0.4 | -0.3 | 0.0 | 0.2 | 0.2 | 0.1 | 0.0 | 0.2 | 0.2 | 1.0 | -0.6 | -1.0 |
| | $e_2$ | 5.5 | 5.7 | 7.4 | 7.6 | 7.8 | 7.9 | 7.9 | 8.0 | 7.7 | 6.9 | 4.8 | 4.3 |

*Table 6.* The same as in Table 5 but for the year 2005

| Station | Parameter | Jan | Feb | Mar | Apr | May | Jun | Jul | Aug | Sep | Oct | Nov | Dec |
|---|---|---|---|---|---|---|---|---|---|---|---|---|---|
| **Rafah** | $n$ | 6.5 | 8.6 | 8.8 | 10.1 | 11.1 | 12 | 11.9 | 11.4 | 10.2 | 9.4 | 7.9 | 6.6 |
| | $h$ | 37.7 | 45.6 | 56.1 | 68.3 | 78 | 82.3 | 80.3 | 72.4 | 60.7 | 49 | 39.5 | 35.5 |
| | $UVB_m$ | 0.0204 | 0.0366 | 0.0498 | 0.0646 | 0.0721 | 0.0777 | 0.0764 | 0.0704 | 0.0595 | 0.0418 | 0.0277 | 0.0192 |
| | $UVB$ | 0.0207 | 0.0369 | 0.0487 | 0.0635 | 0.0708 | 0.0771 | 0.0750 | 0.0702 | 0.0593 | 0.0408 | 0.0281 | 0.0196 |
| | $UVB_{eg}$ | 0.0216 | 0.0384 | 0.0516 | 0.0670 | 0.0748 | 0.0814 | 0.0793 | 0.0743 | 0.0628 | 0.0425 | 0.0293 | 0.0204 |
| | $e_1$ | -1.7 | -1.0 | 2.2 | 1.8 | 1.9 | 0.8 | 1.8 | 0.2 | 0.4 | 2.3 | -1.4 | -1.9 |
| | $e_2$ | -5.9 | -5.0 | -3.6 | -3.8 | -3.7 | -4.8 | -3.9 | -5.6 | -5.5 | -1.8 | -5.8 | -6.3 |
| **Hurghada** | | | | | | | | | | | | | |
| | $n$ | 8.6 | 8.5 | 9.5 | 10.2 | 11.3 | 12 | 11.9 | 11.8 | 10.7 | 10.1 | 9.9 | 9 |
| | $h$ | 41.5 | 49.4 | 59.9 | 72.1 | 81.8 | 86.1 | 81.1 | 76.2 | 64.5 | 52.8 | 43.3 | 39.2 |
| | $UVB_m$ | 0.0312 | 0.0391 | 0.0548 | 0.0668 | 0.0738 | 0.0773 | 0.0758 | 0.0744 | 0.0653 | 0.0458 | 0.0382 | 0.0310 |
| | $UVB$ | 0.0297 | 0.0377 | 0.0539 | 0.0651 | 0.0718 | 0.0766 | 0.0743 | 0.0727 | 0.0633 | 0.0438 | 0.0365 | 0.0295 |
| | $UVB_{eg}$ | 0.0333 | 0.0414 | 0.0578 | 0.0694 | 0.0766 | 0.0818 | 0.0795 | 0.0778 | 0.0678 | 0.0484 | 0.0409 | 0.0334 |
| | $e_1$ | 4.9 | 3.7 | 1.6 | 2.5 | 2.8 | 1.0 | 1.9 | 2.3 | 3.1 | 4.3 | 4.6 | 4.7 |
| | $e_2$ | -6.9 | -5.8 | -5.4 | -4.0 | -3.7 | -5.7 | -4.8 | -4.5 | -3.8 | -5.8 | -7.0 | -7.8 |
| **South Valley** | | | | | | | | | | | | | |
| | $n$ | 8.8 | 8.9 | 9.9 | 10.4 | 11.8 | 12.6 | 12.4 | 12.2 | 10.9 | 10.1 | 9.5 | 8.3 |
| | $h$ | 42.6 | 50.6 | 61 | 73.3 | 82.9 | 87.2 | 82 | 77.3 | 65.7 | 53.9 | 44.5 | 40.5 |
| | $UVB_m$ | 0.0369 | 0.0456 | 0.0632 | 0.0736 | 0.0831 | 0.0881 | 0.0881 | 0.0845 | 0.073 | 0.0524 | 0.0419 | 0.0329 |
| | $UVB$ | 0.0377 | 0.0464 | 0.0634 | 0.0736 | 0.0821 | 0.0876 | 0.0851 | 0.0831 | 0.0724 | 0.0518 | 0.0427 | 0.0340 |
| | $UVB_{eg}$ | 0.0350 | 0.0441 | 0.0605 | 0.0709 | 0.0792 | 0.0847 | 0.0821 | 0.0801 | 0.0695 | 0.0493 | 0.0401 | 0.0313 |
| | $e_1$ | -2.2 | -1.9 | -0.3 | 0.0 | 1.2 | 0.5 | 3.5 | 1.7 | 0.8 | 1.1 | -2.1 | -3.3 |
| | $e_2$ | 5.1 | 3.3 | 4.3 | 3.6 | 4.6 | 3.8 | 6.8 | 5.2 | 4.8 | 5.9 | 4.3 | 4.8 |
| **Aswan** | | | | | | | | | | | | | |
| | $n$ | 9.6 | 9.8 | 10.2 | 10.9 | 12 | 12.8 | 12.6 | 12.4 | 11 | 10.7 | 10.1 | 9.1 |
| | $h$ | 44.3 | 52.5 | 63 | 75 | 83.8 | 87.8 | 83.8 | 78.7 | 68.9 | 57.6 | 47.6 | 42.6 |
| | $UVB_m$ | 0.0417 | 0.0520 | 0.0683 | 0.0804 | 0.0875 | 0.0931 | 0.0915 | 0.0888 | 0.0786 | 0.0579 | 0.0471 | 0.0373 |
| | $UVB$ | 0.0422 | 0.0525 | 0.0684 | 0.0800 | 0.0871 | 0.0931 | 0.0905 | 0.0885 | 0.0777 | 0.0582 | 0.0480 | 0.0384 |
| | $UVB_{eg}$ | 0.0398 | 0.0494 | 0.0633 | 0.0751 | 0.0815 | 0.0873 | 0.0849 | 0.0821 | 0.0738 | 0.0545 | 0.0451 | 0.0363 |
| | $e_1$ | -1.2 | -0.9 | -0.1 | 0.5 | 0.5 | 0.0 | 1.1 | 0.3 | 1.1 | -0.5 | -1.8 | -2.9 |
| | $e_2$ | 4.5 | 4.9 | 7.3 | 6.6 | 6.9 | 6.2 | 7.2 | 7.5 | 6.1 | 5.8 | 4.3 | 2.5 |

Therefore, it could be concluded that, as it was expected, the above Egypt's formula (Eq. (9)) is valid to compute the UV-B solar radiation with high accuracy during cold and hot months at any locations in Egypt. This is due to the modified formulae characterized by simplicity and independence of meteorological parameters, which in turn precisely estimates UV-B radiation at any localitions in Egypt during all months.

*Table 7*. Annual mean values of $UVB_m$, $UVB$, $UVB_{eg}$, $e_1$, and $e_2$ at the four stations

| Parameter | El-Arish | | Hurghada | | S. Valley | | Aswan | |
|---|---|---|---|---|---|---|---|---|
| | 2003 | 2004 | 2003 | 2004 | 2003 | 2004 | 2003 | 2004 |
| $UVB_m$ | 0.0517 | 0.0514 | 0.0556 | 0.0561 | 0.0632 | 0.0636 | 0.0677 | 0.0687 |
| $UVB$ | 0.0512 | 0.0509 | 0.0542 | 0.0546 | 0.0633 | 0.0633 | 0.0677 | 0.0687 |
| $UVB_{eg}$ | 0.0539 | 0.0536 | 0.0586 | 0.0590 | 0.0605 | 0.0606 | 0.0629 | 0.0644 |
| $e_1$ | 0.8 | 0.5 | 2.9 | 3.1 | -0.6 | -0.1 | 0.0 | -0.3 |
| $e_2$ | -4.2 | -4.6 | -5.7 | -5.4 | 4.2 | 4.7 | 6.8 | 5.8 |

### *4.3. UV-B radiation distribution over Egypt*

The monthly mean of measured $n$ values at forty selected stations have been taken from the Egyptian Meteorological Authority and used in this study to calculate the corresponding $UVB$ values at these stations applying the Egypt's formulae (Eq. (9)). The stations have been chosen to cover the whole territory of Egypt. The results of calculated UV-B radiation values have been plotted on relevant charts (*Figs. 4* and *5*). The charts have been carried out by using the SURFER program with the interpolation technique of minimum curvature.

These charts (*Figs. 4* and *5*) have been analyzed and discussed. The main climatic features of UV-B radiation over Egypt are given below:

- The distribution of UV-B over Egypt depends on the latitude, where its intensity tends to increase in the southward and decrease in the northward direction in Egypt. The monthly mean values of UV-B radiation ranges from the highest value of 0.088 MJ $m^{-2}$ at the southern part of Egypt in June, to the lowest value of 0.02 MJ $m^{-2}$ at the northern part of Egypt in January.
- In Egypt the highest values of UV-B radiation occur in June, when its values range from 0.080 in the north to 0.088 MJ $m^{-2}$ in the southwest part of Egypt.
- In Egypt the lowest values of UV-B radiation occur in January, when its values range from 0.020 in the north to 0.044 MJ $m^{-2}$ in the southwest part of Egypt.

- There is a marked difference between the intensity of UV-B radiation at the northern and southern parts of Egypt, especially in the winter months (namely in January, the difference is 0.02 MJ $m^{-2}$), while this difference decreases gradually to take its minimum in the summer months (namely in June, the difference is 0.008 MJ $m^{-2}$).

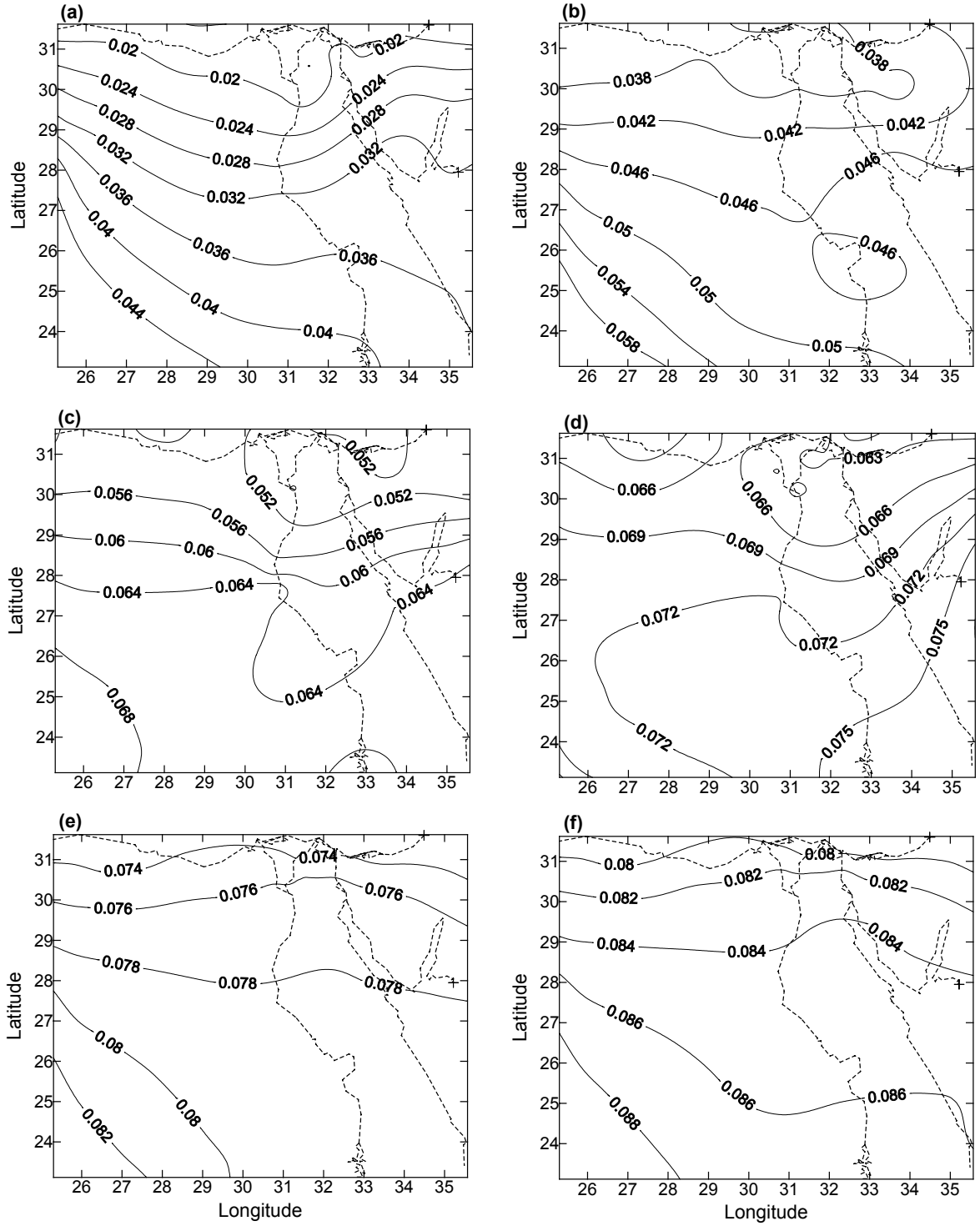


*Fig. 4.* The calculated UV-B values over Egypt during the months (a) January, (b) February, (c) March, (d) April, (e) May, and (f) June.

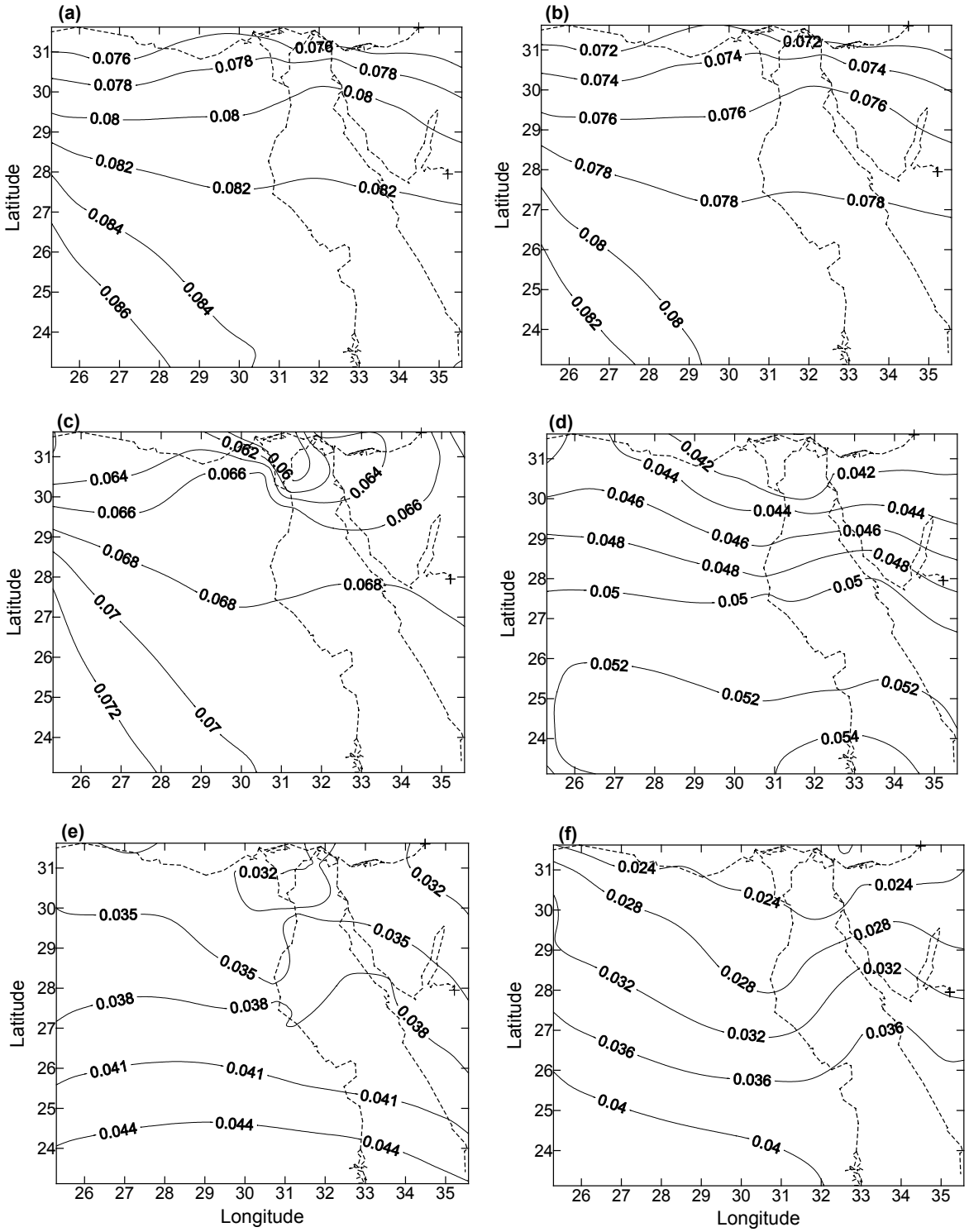


*Fig. 5*. The same as in Fig. 4 but for the months (a) July, (b) August, (c) September, (d) October, (e) November, and (f) December.

## *References*

*Al-Aruri, S., Rasas, M., Al-Jamal, K.,* and *Shaban, N.,* 1988: An assessment of global ultraviolet radiation in the range (0.290-385 μm) in Kuwait. *Sol. Energy 41*, 159-162.

*Barbaro, S., Coppolino, S., Leone, C.,* and *Sinagra, E.*, 1978: Global solar radiation in Italy. *Sol. Energy 20*, 431-435.

*Biswas, A.K.*, 1979: *The Ozone Layer*. Vol. 4. Pergamon Press, Oxford.
*Elhadidy, M.A., Abdel-Nabi, D.Y.,* and *Kruss P.D.*, 1990: Ultraviolet solar radiation at Dhahran, Saudi Arabia. *Sol. Energy 44*, 315-319.
*El-Metwally, M.*, 2004: Simple new methods to estimate global solar radiation based on meteorological data in Egypt. *Atmos. Res. 69*, 217–239.
*Feister, U.* and *Grasnick, K.H.*, 1992: Solar UV radiation measurements at Potsdam (52°22′N, 31°5′E). *Sol. Energy 49*, 541-548.
*Giese, A.C.*, 1982: *Living with our Suns' Ultraviolet Rays*. Plenum Press, New York.
*Khogali, A.*, 1983: Solar radiation over Sudan-comparison of measured and predicted data. *Sol. Energy 31*, 45-53.
*Kirchhoff, V.W., Silva, A.,* and *Pinheiro, K.*, 2002: Wavelength dependence of aerosol optical thickness in the UV-B band. *Geophys. Res. Lett. 29*, 1620, doi:10.1029/2001.
*Kylling, A., Dahlback A.,* and *Mayer, B.*, 2000. The effect of clouds and surface albedo on UV irradiances at a high latitude site. *Geophys. Res. Lett. 27*, 1411-1414.
*Luccini, E., Cede, A.*, and *Piacentini, R.D.*, 2003: Effect of clouds on UV and total irradiance at Paradise Bay, Antarctic Peninsula, from a summer 2000 campaign. *Theor. Appl. Climatol. 75*, 105-116.
*McKenzie, R.L., Blumthaler M., Booth, C.R., Diaz, S.B., Frederick, J.E., Ito, T., Madronich, S.,* and *Seckmeyer, G.*, 1995: Surface ultraviolet radiation. In *Scientific Assessment of Ozone Depletion*. WMO Global Ozone Research and Monitoring Project Report No. 37, 9, 1-9. 22.
*Parrish, J.A., Rox Arderson, R., Urbach, F.,* and *Pitts, D.*, 1978: *UV-A*. Plenum Press, New York.
*Robaa, S.M.*, 2003: On the estimation of global and diffuse solar radiation over Egypt. *Mausam 54*, 17-35.
*Robaa, S.M.*, 2005: A study of ultraviolet solar radiation at Cairo urban area, Egypt. *Idojaras 109*, 123-138.
*Robaa, S.M.* and *Hafez, Y.Y.*, 2006: Study the teleconection between the variations of total ozone values over Egypt and climatic indices NAO and SOI. *J. Environ. Sci. 4*, 70-85.
*Salem, A.I.*, 2000: Analysis and correlation of ultraviolet solar radiation from routine meteorological measurements over Egypt. *Mausam 51*, 275-280.
*Sivkov, S.I.*, 1964. To the methods of computing possible radiation in Italy. *Trans. Main Geophys. Obs*. 160.
*Som, A.K.*, 1992: Solar UV-B radiation measurements over Bahrain. *Renew. Energ. 2*, 93-98.
*Tang, X., Madronich, S., Wallington, T.,* and *Calamari, D.*, 1998: Changes in tropospheric composition and air quality. *J. Photoch. Photobio. B. 46*, 83-95.
*Wang, G.* and *Jianhui, B.*, 1996: Variation in trend of UV radiation in Beijing district. *First Stratospheric Processes and Their Role in Climate*. Melbourne, Australia, 2-6 Dec 1996, Vol. II, WCRP-99 WMO/TD-NO. 814.
*WMO*, 1990: *Guide to Meteorological Observations Methods*. Tn-8, Geneva, Switzerland, Chapter 9. WMO Secretariat, 925–932.
*WRC*, 1985: Sixth international pyreheliometer comparison (IPC VI), 1-18 October. *Working Report,* No. 137, Davos, Switzerland.
*WRC*, 1995: International pyreheliometer comparison (IPC VII), 25 September-13 October. *Working Report,* No. 188, Davos, Switzerland.
*Wuttke, S., Verdebout, J.,* and *Seckmeyer, G.*, 2003: An improved algorithm for satellite derived UV radiation. *Photochem. Photobiol.* 77, 52-57.
*Zerefos, C.S., Balis, D., Tzortziou, M., Bais, A., Tourpali, K., Meleti, C., Bernhard, G.,* and *Herman, J.*, 2001: A note on the interannual variation of UV-B erythemal doses and solar irradiance from ground – based and satellite observations. *Ann. Geophys. 19*, 115-120.

# BOOK REVIEW

*Geoffrey K. Vallis:* **Atmospheric and Oceanic Fluid Dynamics: Fundamentals and Large-scale Circulation**. Cambridge University Press, 2006, 745 pages, 16 chapters.

*Geoffrey K. Vallis* condensed his great teaching experience into the textbook on atmospheric and oceanic dynamics. The material is divided into four major parts: (i) fundamentals of geophysical fluid dynamics, (ii) instabilities, wave-mean flow interaction, and turbulence, (iii) large-scale atmospheric, and (iv) large-scale oceanic circulation.

The introductory part, starting from classical concepts of fluid dynamics and thermodynamics, studies the effects of rotation and stratification, shallow water, geostrophic and quasi-geostrophic flow systems, vorticity and potential vorticity, as well as the Rossby waves. The second part guides the reader through barotropic and baroclinic instability, wave-mean flow interaction, theory of incompressible and geostrophic turbulence. Moreover, this part is closed with discussion of turbulent diffusion and eddy transport. The third part is focused on large scale atmospheric circulation: the overturning circulation (Hadley and Ferrel cells), zonally averaged mid-latitude atmospheric circulation, and planetary waves. The subject of the closing part is the wind- and buoyancy-driven as well as simultaneous wind- and buoyancy-driven ocean circulation. Each chapter was designed to form self-contained unit.

The text was written to satisfy the requirements of graduate courses, and it is readable. The basic material was supplemented with parts which contain advanced mathematical derivations, which may be omitted on first reading, and discuss modern research topics. The chapters end with very useful notes, including a short biography of the scientists who have made major contributions to the studied fields, list of further reading, and set of unsolved problems. The author appeals to the readers to post their own problem solutions and to extend the currently very poor set of solutions published on the web site associated with the book. All the figures, many in color, the errata, and the ongoing discussion may be downloaded from the web site.

The book represents a comprehensive survey on the theory of geophysical fluid dynamics, large-scale atmospheric and oceanic dynamics combining needs of graduate students and researchers too. It has the potential to become the standard reference for modern topics of the atmospheric and oceanic dynamics including climate systems.

*Á. Bordás*

# GUIDE FOR AUTHORS OF *IDŐJÁRÁS*

The purpose of the journal is to publish papers in any field of meteorology and atmosphere related scientific areas. These may be

- research papers on new results of scientific investigations,
- critical review articles summarizing the current state of art of a certain topic,
- short contributions dealing with a particular question.

Some issues contain "News" and "Book review", therefore, such contributions are also welcome. The papers must be in American English and should be checked by a native speaker if necessary.

Authors are requested to send their manuscripts to

*Editor-in Chief of IDŐJÁRÁS*
*P.O. Box 39, H-1675 Budapest, Hungary*

in three identical printed copies including all illustrations. Papers will then be reviewed normally by two independent referees, who remain unidentified for the author(s). The Editor-in-Chief will inform the author(s) whether or not the paper is acceptable for publication, and what modifications, if any, are necessary.

Please, follow the order given below when typing manuscripts.

*Title part:* should consist of the title, the name(s) of the author(s), their affiliation(s) including full postal and e-mail address(es). In case of more than one author, the corresponding author must be identified.

*Abstract:* should contain the purpose, the applied data and methods as well as the basic conclusion(s) of the paper.

*Key-words:* must be included (from 5 to 10) to help to classify the topic.

*Text:* has to be typed in single spacing with wide margins on one side of an A4 size white paper. Use of S.I. units are expected, and the use of negative exponent is preferred to fractional sign. Mathematical formulae are expected to be as simple as possible and numbered in parentheses at the right margin.

All publications cited in the text should be presented in a *list of references*, arranged in alphabetical order. For an article: name(s) of author(s) in Italics, year, title of article, name of journal, volume, number (the latter two in Italics) and pages. E.g., *Nathan, K.K.,* 1986: A note on the relationship between photo-synthetically active radiation and cloud amount. *Időjárás 90,* 10-13. For a book: name(s) of author(s), year, title of the book (all in Italics except the year), publisher and place of publication. E.g., *Junge, C.E.,* 1963: *Air Chemistry and Radioactivity.* Academic Press, New York and London. Reference in the text should contain the name(s) of the author(s) in Italics and year of publication. E.g., in the case of one author: *Miller* (1989); in the case of two authors: *Gamov* and *Cleveland* (1973); and if there are more than two authors: *Smith et al.* (1990). If the name of the author cannot be fitted into the text: (*Miller*, 1989); etc. When referring papers published in the same year by the same author, letters a, b, c, etc. should follow the year of publication.

*Tables* should be marked by Arabic numbers and printed in separate sheets with their numbers and legends given below them. Avoid too lengthy or complicated tables, or tables duplicating results given in other form in the manuscript (e.g., graphs)

*Figures* should also be marked with Arabic numbers and printed in black and white in camera-ready form in separate sheets with their numbers and captions given below them. TIF, GIF or BMP formats should be used for electronic artwork submission.

*The text* should be submitted both in manuscript and in electronic form, the latter in e-mail or CD. MS Word format is preferred.

*Reprints:* authors receive 30 reprints free of charge. Additional reprints may be ordered at the authors' expense when sending back the proofs to the Editorial Office.

*More information for authors is available:*
antal.e@met.hu

Published by the Hungarian Meteorological Service

Budapest, Hungary

**INDEX 26 361**

**HU ISSN 0324-6329**